iScience

CellPress
OPEN ACCESS

Article

CD38 regulates ovarian function and fecundity via NAD^+ metabolism

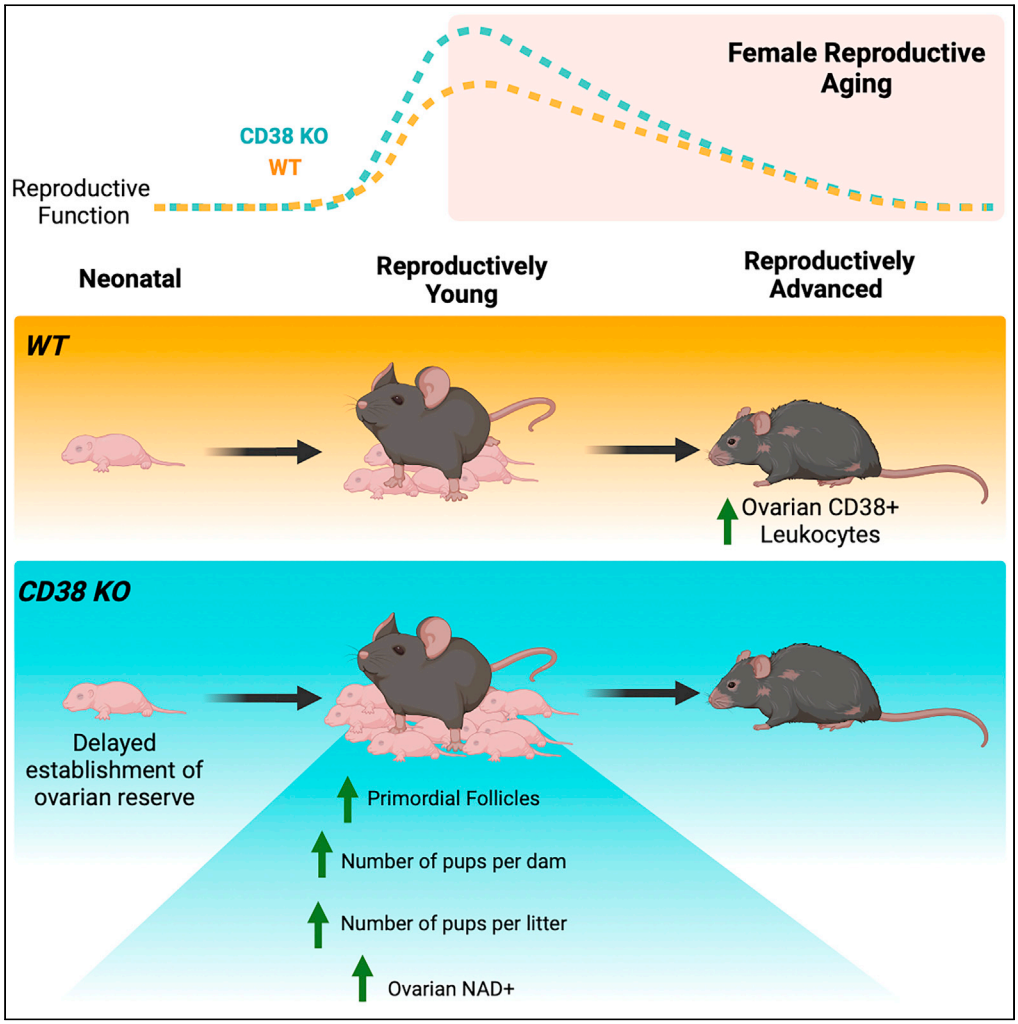

Rosalba Perrone, Prasanna Vadhana Ashok Kumaar, Lauren Haky, ..., Morten Scheibye-Knudsen, Francesca E. Duncan, Eric Verdin

f-duncan@northwestern.edu (F.E.D.)
everdin@buckinstitute.org (E.V.)

Highlights

Ovarian CD38 expression is extrafollicular and increases with reproductive age

CD38 loss results in elevated ovarian NAD+ and increased fecundity in young mice

CD38 loss is associated with a higher initial ovarian reserve in young mice

An extended follicle formation period in CD38 KO mice underlies the larger reserve

Perrone et al., iScience *26*, 107949
October 20, 2023
https://doi.org/10.1016/j.isci.2023.107949

iScience

CellPress
OPEN ACCESS

Article

CD38 regulates ovarian function and fecundity via NAD+ metabolism

Rosalba Perrone,[1,5] Prasanna Vadhana Ashok Kumaar,[1,5] Lauren Haky,[1,2,5] Cosmo Hahn,[1] Rebeccah Riley,[1] Julia Balough,[1] Giuliana Zaza,[1] Bikem Soygur,[1] Kaitlyn Hung,[1] Leandro Prado,[1] Herbert G. Kasler,[1] Ritesh Tiwari,[1] Hiroyuki Matsui,[1] Genesis Vega Hormazabal,[1] Indra Heckenbach,[3] Morten Scheibye-Knudsen,[3] Francesca E. Duncan,[1,4,*] and Eric Verdin[1,6,*]

SUMMARY

Mammalian female reproductive lifespan is typically significantly shorter than life expectancy and is associated with a decrease in ovarian NAD+ levels. However, the mechanisms underlying this loss of ovarian NAD+ are unclear. Here, we show that CD38, an NAD+ consuming enzyme, is expressed in the ovarian extrafollicular space, primarily in immune cells, and its levels increase with reproductive age. Reproductively young mice lacking CD38 exhibit larger primordial follicle pools, elevated ovarian NAD+ levels, and increased fecundity relative to wild type controls. This larger ovarian reserve results from a prolonged window of follicle formation during early development. However, the beneficial effect of CD38 loss on reproductive function is not maintained at advanced age. Our results demonstrate a novel role of CD38 in regulating ovarian NAD+ metabolism and establishing the ovarian reserve, a critical process that dictates a female's reproductive lifespan.

INTRODUCTION

The ovary is a dynamic organ consisting of heterogeneous cell types that must function coordinately to enable female reproductive function. In mammals, the ovarian reserve or number of primordial follicles that dictates the reproductive lifespan is established early in development and is considered finite and non-renewable. The ovarian reserve undergoes a natural winnowing over time combined with diminished egg quality, which together contribute to decreased fertility in females by their late 30s and eventual complete cessation of reproductive function at menopause.[1]

Cells within the ovary require energy to maintain homeostasis to support folliculogenesis.[2] Nicotinamide adenine dinucleotide (NAD+) is a cofactor, co-substrate, and redox partner in important metabolic pathways involved in energy generation, cell signaling, and tissue repair.[3] NAD+ regulates energy metabolism in several ovarian cells, including oocytes, granulosa cells, and theca cells, which orchestrate folliculogenesis, oocyte maturation, and ovulation.[4,5] During ovulation, there is a high demand for NAD+ to support follicular rupture, cumulus-oocyte complex release, and corpus luteum formation. NAD+ also contributes to DNA damage repair which is critical for the prevention of chromosomal abnormalities and maintenance of genetic integrity.[6] Considering the central role of NAD+ in mediating ovarian metabolism and henceforth function, it is not surprising that there is a strong association between decline in ovarian NAD+ levels and loss of ovarian function.

NAD+ homeostasis is maintained by a "supply-demand" chain, in which NAD+ is replenished by biosynthetic pathways to counter its utilization by NAD+-dependent metabolic pathways.[2,3] However, over time, this balance tips toward the latter due to increased demand for NAD+ under survival circumstances, such as the constant need for DNA repair caused by cumulative oxidative stress.[7,8] The decline in NAD+ with chronological aging has been reported in several organs, such as the liver and adipose, and is detrimental to physiological processes leading to metabolic dysfunction and age-associated diseases.[9] In the ovary, NAD+ levels also decline with age, and this reduction is associated with a decrease in gamete quantity and quality.[10–12] Supplementation with NAD+ precursors, such as nicotinamide mononucleotide (NMN) or nicotinamide riboside (NR), increase NAD+ levels and improve gamete quality, ovarian function, and fertility in aged mice.[10–13] These findings suggest a key role for NAD+ metabolism in ovarian function and reproductive aging. However, the molecular mechanisms regulating ovarian NAD+ loss have not been elucidated.

The age-related decrease in NAD+ levels is not solely attributed to an increased demand for NAD+ but also to an increase in NAD+ degradation.[14] One of the potential factors contributing to the NAD+ deficit during aging is the glycoprotein NADase, CD38, which catalyzes the

[1]Buck Institute for Research on Aging, Novato, CA, USA
[2]The Dominican University of California, San Rafael, CA, USA
[3]Center for Healthy Aging, Department of Cellular and Molecular Medicine, University of Copenhagen, Copenhagen, Denmark
[4]Department of Obstetrics and Gynecology, Feinberg School of Medicine, Northwestern University, Chicago, IL, USA
[5]These authors contributed equally
[6]Lead contact
*Correspondence: f-duncan@northwestern.edu (F.E.D.), everdin@buckinstitute.org (E.V.)
https://doi.org/10.1016/j.isci.2023.107949

breakdown of NAD+ into nicotinamide (NAM) and ADP-ribose (ADPR).[15,16] CD38 mediates key cellular functions, from regulating immune cell function as a surface receptor on specific innate and acquired immune cells to modulating metabolic processes through its hydrolase and cyclase activities.[17,18] However, an age-associated increase in CD38 expression and activity in multiple tissues, such as the liver, adipose, and skeletal muscle, negatively correlates with tissue NAD+ levels, corroborating its role in age-associated cellular dysfunction.[19,20] Although there is existing research on CD38's role in aging and age-related diseases,[21–23] its role in female reproductive function and aging has not been systematically investigated.

In the current study, we demonstrate that CD38 is expressed in the mouse ovary primarily in the extrafollicular compartment with enrichment in immune cells. Ovarian CD38 increases with age, and interestingly, our findings using a genetic loss-of-function model demonstrate that CD38 is a negative regulator of reproductive function in reproductively adult females. Reproductively young female mice lacking CD38 exhibit a larger number of ovarian follicles and increased fecundity, and these phenotypes are associated with higher ovarian NAD+ levels. The increased number of follicles appears to be due to the role of CD38 in modulating ovarian reserve formation early in development. Overall, our findings highlight the role of CD38 in regulating ovarian function and fertility through NAD+ metabolism. Targeting CD38 or its downstream effects on NAD+ metabolism may offer new approaches to enhance reproductive longevity.

RESULTS

CD38 is expressed in extrafollicular cells in the ovary and its expression increases with age

The ovary is a heterogeneous tissue that is constantly subject to remodeling due to folliculogenesis, ovulation, and corpus luteum formation and regression.[24] The ovary includes multiple cell types, including granulosa, mesenchymal, endothelial, epithelial, immune cells, and oocytes, and the specific composition is highly dependent on animal age and cycle stage.[25]

To determine where CD38 is expressed in the ovary, we visualized and quantified *Cd38* transcripts in specific ovarian subcompartments in reproductively adult mice (Figure 1A). Cells within extrafollicular subcompartments expressed high levels of *Cd38* transcript, including the ovarian surface epithelium (OSE), the stroma, the vasculature, and the corpora lutea (CL) (Figure 1B). Interestingly, follicles at all stages of development exhibited minimal to no *Cd38* expression both in the oocyte and somatic granulosa cells (Figure 1C). Computational image analysis in which *Cd38* mRNA transcript number in each subcompartment was normalized to subcompartment area confirmed that ovarian *Cd38* expression was primarily extrafollicular with CL and vascular compartments having the highest levels of *Cd38* transcription when compared to OSE and ovarian follicles (Figure 1D).

CD38 protein expression largely paralleled its transcripts (Figure 1E), localizing mainly to the ovarian stroma, the vasculature, the CL, the regressing CL, and the atretic follicles (Figure 1F). There was minimal to no expression in the OSE (Figure 1F). Follicles at all stages of development lacked CD38 protein expression in both the germ cell and granulosa cell compartments, but there appeared to be expression in the vascular region of the theca layer (Figure 1G). Overall, CD38 protein localization was consistent with what was observed with the transcripts.

CD38 expression increases with age in several mouse tissues, including the liver, adipose, spleen, and skeletal muscle.[26] To investigate how CD38 levels change with age in ovaries, we extracted whole tissue lysate from reproductively young (2 months) and old (20 months) mouse ovaries and evaluated total CD38 protein content via western blot. We observed a more than 2-fold increase in CD38 protein levels with age (Figures 1H and 1I). These findings are consistent with a previously published transcriptomic dataset in which an increase in *Cd38* transcript levels is observed in mouse ovaries at 15 and 18 months of age[27] (Figure 1J).

CD38 KO animals have low NADase activity and increased ovarian NAD+ levels

An age-dependent increase in CD38 expression causes NAD+ level depletion in multiple tissues, and a total body knock-out mouse model of CD38 (CD38 KO) is protected from NAD+ loss.[26] Although previous research has documented a decline in ovarian NAD+ levels,[10,11] the role of CD38 in this process is unknown. Therefore, we investigated the impact of CD38 on ovarian NAD+ regulation. To this end, we collected ovaries from WT females at different ages (2 months; young, 7 months; middle age, 12 months; advanced age) and measured NAD+ consumption in whole ovarian lysates using a fluorescence-based NADase assay.[28] Our data showed an age-dependent increase in NAD+ degradation (Figure 2A). This NADase activity was dependent on CD38 as minimal activity was observed in ovaries from 2 month old CD38 KO mice from a separate mouse colony bred as homozygotes (Figure 2A). To further demonstrate that the observed NADase activity was CD38-dependent, we treated the WT ovarian lysates with the highly specific CD38 inhibitor, 78c,[20] which resulted in near complete suppression of NAD+ hydrolysis (Figure 2B).

To further characterize the NAD+-related ovarian metabolomic profile, we collected ovaries from WT and CD38 KO virgin females at different reproductive ages (2 months; young, 6 months; middle age, 12 months; advanced age) and post-fertile age (20 months) and measured NAD+ and related metabolites (NAM and ADPR) using mass spectrometry. Ovaries from CD38-deficient mice harbored significantly higher NAD+ levels than ovaries from age-matched WT mice, particularly at 2 and 6 months (Figure 2C). However, at 20 months of age, NAD+ levels in ovaries from CD38 KO mice declined to levels comparable to those of WT controls, indicating that CD38 deficiency did not offer protection from NAD+ loss during physiologic ovarian aging (Figure 2C). Notably, ovaries from CD38 KO mice had relatively lower levels of NAM (Figure 2D) and ADPR (Figure 2E) compared to age-matched WT controls. These are both primary products of CD38-dependent NAD+ hydrolysis, thus highlighting the specific effect of CD38 on ovarian NAD+ metabolism. Our findings suggested a key role for CD38 in regulating and maintaining NAD+ homeostasis in the ovary.

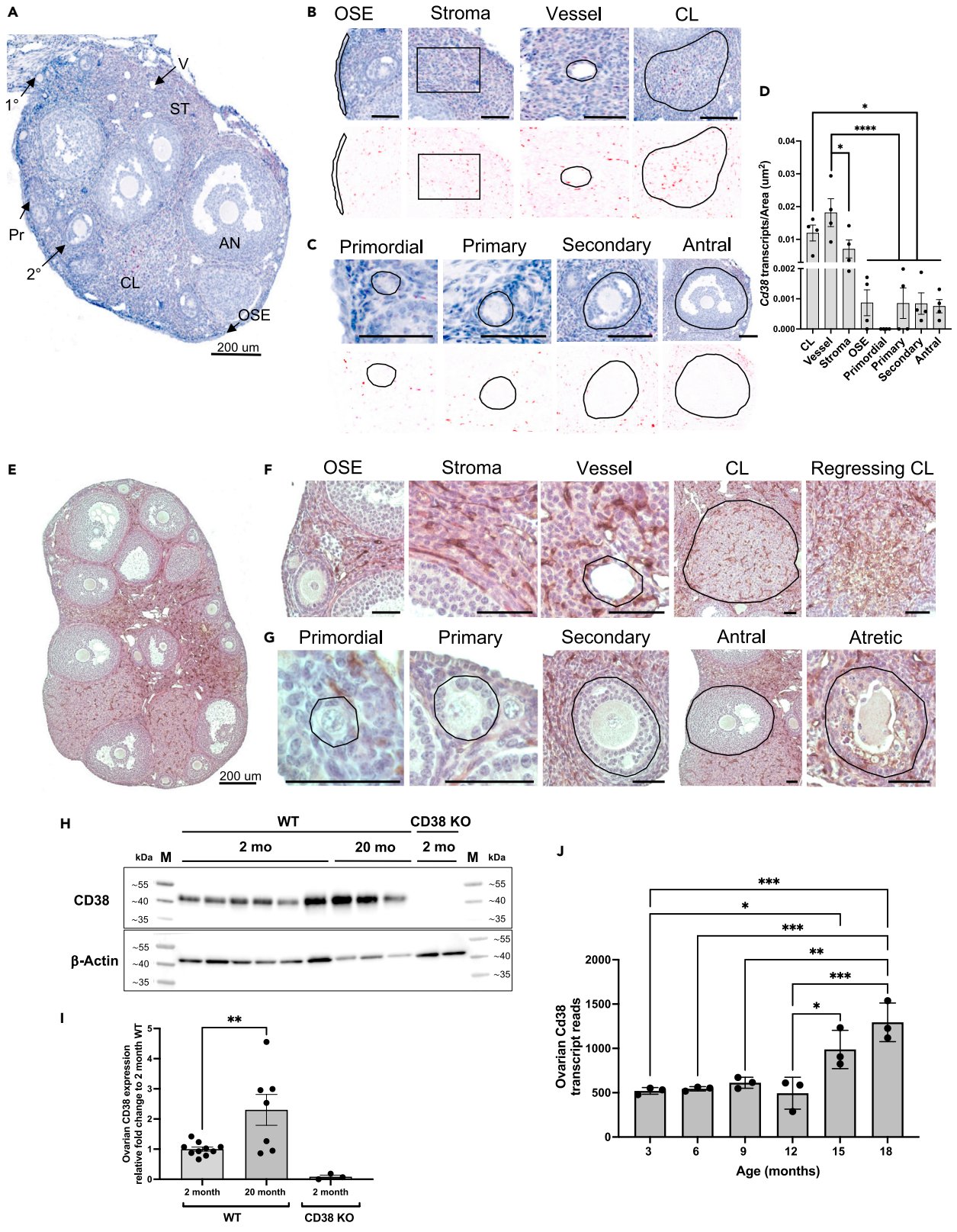
A
V
1°
ST
Pr
AN
2°
CL
OSE
200 um
B
OSE
Stroma
Vessel
CL
C
Primordial
Primary
Secondary
Antral
D
Cd38 transcripts/Area (um²)
CL
Vessel
Stroma
OSE
Primordial
Primary
Secondary
Antral
E
200 um
F
OSE
Stroma
Vessel
CL
Regressing CL
G
Primordial
Primary
Secondary
Antral
Atretic
H
WT
CD38 KO
2 mo
20 mo
2 mo
kDa
M
CD38
β-Actin
I
Ovarian CD38 expression relative fold change to 2 month WT
2 month
20 month
2 month
WT
CD38 KO
J
Ovarian Cd38 transcript reads
Age (months)

Figure 1. CD38 is expressed in the extrafollicular regions of the mouse ovary and it increases with age

(A) Localization of CD38 mRNA by *in situ* hybridization (RNAscope) in 2-month-old ovarian section from WT mouse, 200 μm scale.

(B) Representative higher magnification images from (A) showing CD38 mRNA localization by RNA Scope in OSE, stroma, vessel and CL. 50 μm scale unless otherwise indicated.

(C) Representative higher magnification images from (A) showing CD38 mRNA localization by RNA Scope in ovarian follicles at different developmental stages. 50 μm scale unless otherwise indicated.

(D) Quantification of CD38 mRNA localization by RNA Scope in ovarian structures and regions (n = 4). (One-Way ANOVA statistical analysis, * = $p < 0.05$, **** = $p < 0.00005$). Data are represented as mean ± SEM.

(E) Representative image showing localization of CD38 protein by immunohistochemistry (IHC) in 2-month-old ovarian section from WT mouse, 200 μm scale.

(F) Representative higher magnification images showing CD38 protein localization in OSE, stroma, vessel, CL and regressing CL by immunohistochemistry (IHC) in 2-month-old ovarian section from WT mouse, 50 μm scale unless otherwise indicated.

(G) Representative higher magnification images of CD38 protein localization by IHC in ovarian follicles at different developmental stages, 50 μm scale unless otherwise indicated.

(H and I) (H) Representative western blot of CD38 expression in whole ovarian tissue lysate from 2 months (n = 6) and 20 months (n = 3) old WT mice. Whole ovarian tissue lysate from 2 months old CD38 KO animals (n = 2) was used as control. ***β***-actin was used as housekeeping loading control. M corresponds to the prestained protein ladder used as kDa size standards (I) Bar chart from 3 independent western Blot experiments showing CD38 expression in whole ovarian tissue lysate from 2 months to 20 months old WT mice. Whole ovarian tissue lysate from 2 months old CD38 KO animals was used as control. ***β***-actin was used as housekeeping loading control. (Unpaired T Test statistical analysis, ** = $p < 0.005$). Data are represented as mean ± SEM.

(J) Cd38 transcript reads in 3, 6, 9, 12, 15, and 18 month old mouse ovaries (n = 3). (One-Way ANOVA statistical analysis, * = $p < 0.05$, ** = $p < 0.005$, *** = $p < 0.0005$). Data are represented as mean ± SD. See also Figure S1. (OSE, ovarian surface epithelium; CL, corpus luteum).

CD38 is enriched in ovarian immune cells and its expression in leukocytes increases with reproductive age

CD38 transcript and protein were highly expressed in the ovarian stroma, which is heterogeneous in cell type composition, containing populations including fibroblasts, immune cells, endothelial cells, and smooth muscle cells.[29] To gain a better understanding of cell type-specific *Cd38* expression in the ovary, we interrogated the Mouse Cell Atlas (MCA) which contains transcriptomic data of mouse tissues at single-cell resolution.[30] *Cd38* was highly expressed in ovarian endothelial cells and macrophages,[30] which is consistent with localization in other tissues.[22] To further examine CD38 expression in ovarian endothelial cells and macrophages, we performed co-labeling in ovarian histological sections with antibodies against CD38 and either CD31 (endothelial cell marker) or F4/80 (macrophage cell marker) (Figures S1A and S1B). CD31 expression was enriched in some CLs and in the ovarian stroma as expected given the known localization of vasculature in the ovary (Figure S1A). Only a portion of CD31 expressing cells co-labeled with CD38 within the ovarian stroma and vessels (Figure S1A'). Interestingly, there were distinct populations of both CD38 positive (Figure S1A'') and negative (Figure S1A''') endothelial cells within the CL. Similar to CD31, F4/80 positive cells were mostly localized in the ovarian stroma and the CLs (Figure 2B). The majority of F4/80 expressing cells appeared to be CD38 positive within the ovarian stroma (Figure S2B') and CD38 negative in the CL (Figure S2B''), suggesting heterogeneity of CD38 expression within the ovarian macrophage population. Our results confirmed that CD38 is expressed in a subset of ovarian endothelial cells and macrophages but also demonstrates localization to other cell types within the ovarian microenvironment.

In addition to macrophages, there are many different populations of immune cells in the ovary that undergo dynamic changes during development, the reproductive cycle, and aging.[27,31] In other tissues, CD38 is expressed in several immune populations, including macrophages, NK, T and B cells.[32] CD38 expression on immune cells increases as a result of key immunological responses such as inflammation and infection,[32] and during aging an accumulation of CD38 positive immune cells, in particular macrophages, has been reported in several tissues[22,23] which drives NAD+ depletion and leads to age-associated phenotypes.[20,26]

To further characterize CD38 expression within the ovarian microenvironment during reproductive aging, we performed a flow cytometry-based immune profiling analysis of the mouse ovary across the reproductive lifespan at reproductively young, mid, and advanced ages. We analyzed ovaries from both WT and CD38 KO mice to capture potential cell composition changes in the absence of CD38 (Figure 3A). We identified eleven cell types representing the main populations involved in innate and adaptive immunity (Figure 3B). CD38 was expressed in different immune cell types, primarily macrophages, B cells, NK cells, and T cells (Figure 3C), in line with previously reported evidence in other tissue types.[32] In ovaries from WT mice, approximately 30–40% of the cells expressing CD38 were within the ovarian leukocyte population ($CD45^+$), whereas only approximately 10% of the non-leukocyte ($CD45^-$) cells in the ovary expressed CD38 (Figure 3D). Interestingly, $CD38^+$ leukocytes increased with age, whereas $CD38^+$ cells in the non-leukocyte population did not change (Figure 3D). These data are consistent with our previous data in the liver where CD38 levels increased with age only in Kupffer cells but not in non-immune cells including hepatocytes and endothelial cells.[22] Our results demonstrate that ovarian CD38 is mostly expressed in the immune compartment, and CD38 positive leukocytes specifically increase with reproductive age.

CD38 loss-of-function results in significant changes in the ovarian immune milieu during reproductive aging

Consistent with other reports,[27,33] our data demonstrated that the ovarian immune compartment profoundly shifts with advanced reproductive age (Figure 3E). Ovaries from reproductively young WT mice are enriched in innate immune cells, including macrophages and dendritic cells (DC) which together represent around 60% of the entire ovarian immune landscape (Figure S2A). Interestingly, ovaries from reproductively old mice exhibit a dramatic decrease in innate immunity coupled with an increase in adaptive immunity, in particular T cells (Figure S2A). The age-dependent increase in T cells appeared to be mostly driven by CD4, CD8 double-negative (DN) T cells (Figure S2B).

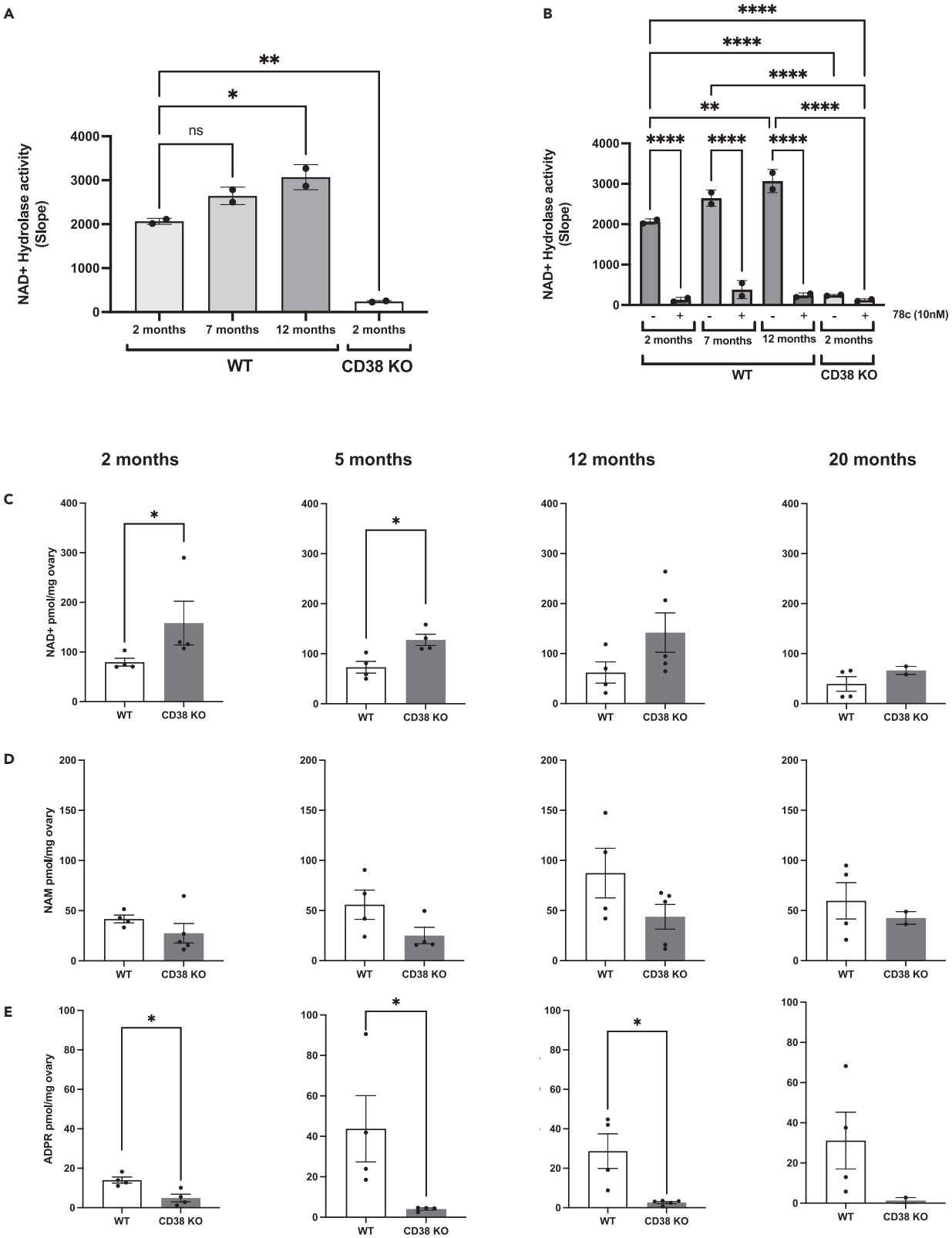
A
NAD+ Hydrolase activity (Slope)
ns
*
**
2 months
7 months
12 months
2 months
WT
CD38 KO
B
NAD+ Hydrolase activity (Slope)
78c (10nM)
2 months
7 months
12 months
2 months
WT
CD38 KO
2 months
5 months
12 months
20 months
C
NAD+ pmol/mg ovary
D
NAM pmol/mg ovary
E
ADPR pmol/mg ovary
WT
CD38 KO

Figure 2. CD38 regulates ovarian NAD+ metabolism

(A) Quantification of ovarian NAD+ hydrolase activity from whole ovarian lysates of 2, 7, and 12 month old WT and 2 month old CD38 KO mice (n = 2/group, two ovaries per n; One-Way ANOVA statistical analysis, * = $p < 0.05$, ** = $p < 0.005$). Data are represented as mean ± SD.

(B) Quantification of ovarian NAD+ hydrolase activity and suppression with the CD38 inhibitor 78c from 2, 7, and 12 month old WT and 2 month old CD38 KO mice (n = 2/group, two ovaries per n; One-Way ANOVA statistical analysis, ** = $p < 0.005$ *** = $p < 0.0005$, **** = $p < 0.00005$). Data are represented as mean ± SD.

(C–E) LCMS quantification of (C) NAD+, (D) NAM, and (E) ADPR levels in whole ovary extracts of 2, 6, 12, and 20 months old WT and CD38 KO mice (n = 2–5 per group, Mann-Whitney t-test, * = $p < 0.05$). Data are represented as mean ± SEM.

Significant age-related changes in the immune milieu were also observed in ovaries from CD38 KO mice (Figure 3F) with overall similar trends in reduced innate immunity and increased adaptive immunity (Figure S2C). The main adaptive population that increased with age in ovaries from CD38 KO mice was the DN T cells similar to WT controls (Figure S2D). Although overall age-dependent trends in immune cell populations were similar across genotypes, CD38 KO mice showed several unique features compared to WT counterparts. Ovaries from WT mice showed an age-dependent increase in total leukocytes. However, no significant differences were observed when compared with the total number of immune cells in CD38 KO ovaries across ages (Figure 3G). Ovaries from WT mice showed an interesting age-dependent decrease in monocytes (Figure 3H) and granulocytes (Figure 3I), but this pattern was not observed in CD38 KO ovaries (Figures 3H and 3I). Innate lymphoid cells (ILCs), another cell type of the innate immunity, significantly increased with age in ovaries from WT mice, but only modest changes in this population were observed with age in ovaries from CD38 KO mice (Figure 3J). Although no significant differences were observed in the monocytes composition between WT and CD38 KO ovaries with age, 12 month old CD38 KO ovaries showed a slight but significant higher amount of granulocytes (Figure 3I) and lower amount of ILCs (Figure 3J). Although the relevance of these immunological changes is unclear, our data might indicate a role of CD38 in regulating ovarian innate immune composition during aging. As for other innate immune cells, an overall age-dependent decrease in total macrophages was observed in both WT and CD38 KO ovaries while no changes in DC occurred in both strains (Figures S2A and S2B). Interestingly, we noticed a change in the macrophage cell composition with a relative increase with age in the monocyte-derived population (CD11c+) versus the tissue-resident (CD11c-) population in both WT and CD38 KO ovaries (Figures S2E and S2F). The same age-related trend in ovarian macrophage composition was previously reported.[27]

In addition to canonical macrophages, a highly penetrant and unique population of macrophage-derived multinucleated giant cells (MNGCs) accumulates with age in the ovary and is associated with chronic inflammation.[34,35] Although this cell population has been demonstrated to express the macrophage marker F4/80 [35], their analysis and quantification with single-cell based techniques, including flow cytometry, is challenging due to their large size and limited survival during cell-dissociation protocols. Histological analysis of MNGCs represents the optimal way to visualize and quantify MNGCs in tissues.[34,35] Given the importance of MNGCs in the context of ovarian aging, we analyzed their presence and relative abundance in ovaries from both CD38 KO and WT mice collected across ages spanning 2 to 28 months (Figure 3K; Figure S2F). As expected, MNGCs were virtually absent in ovaries from reproductively young mice and significantly increased with age (Figure 2L). No significant differences in the amount of MNGCs were observed between the two genotypes up until 12.5 months. However, a significantly larger ovarian area was occupied by MNGCs in ovaries from WT mice at 20 and 28 months relative to age-matched CD38 KO (Figure 3L). Overall, our data seem to suggest a role of CD38 in partially shaping the ovarian immune landscape during ovarian aging.

CD38 loss-of-function results in a larger ovarian reserve and enhanced fecundity in reproductively young mice

The increase of CD38 in the ovary with age is coincident with decreased NAD+ metabolism, a partially altered immune landscape, and reduced reproductive potential, so we hypothesized that a reduction in CD38 may result in enhanced reproductive longevity. Therefore, we investigated reproductive function in CD38 KO mice and validated that CD38 expression was completely eliminated in the ovary (Figures 1H and 1I). Loss of ovarian follicles, and particularly primordial follicles which define the ovarian reserve or reproductive lifespan of an individual, is a primary quantitative metric of reproductive aging.[36] Thus, we classified and quantified follicles in ovarian histological sections from both CD38 KO and WT mice across the reproductive lifespan (Figure 4A). As expected, the number of follicles per ovarian area decreased with age, and this was irrespective of follicle class (Figures 4B–4F). When comparing genotypes, ovaries from CD38 KO mice exhibited a larger number of total follicles per ovarian area at reproductively young time points (2 months and 5 months) compared to WT controls (Figure 4B). This increase was largely due to an increase in primordial follicles or the ovarian reserve (Figure 4C), although there was also a tendency toward an increased number of primary, secondary, and antral follicles per ovarian area in ovaries from CD38 KO mice relative to controls. There were no differences in follicle counts between the two genotypes at 12.5 and 20 months. When examining the proportion of each follicle class across genotypes and ages, a larger fraction of the total follicle pool was composed of primordial follicles in ovaries from CD38 KO mice compared to controls at the reproductively young time points (Figure 4G).

To determine whether the increase in the ovarian reserve in reproductively young CD38 KO mice translated into improved fertility, we performed a standard 6-month breeding trial with WT and CD38 KO females derived from separate litters at three different reproductive ages (young, mid, and advanced) and reproductively active adult WT males of proven fertility (Figure 5A). Readouts included time to achieve first litter, total litters, number of pups per dam and total number of pups per litter (Figures 5B–5E). In addition, since CD38 KO females have been reported to exhibit impaired maternal nurturing due to altered oxytocin regulation,[37] we evaluated the percentage of pups that survived prior to weaning (Figure S3A). In the breeding trial, the time it took to achieve the first litter increased with age consistent with an age-dependent decline in reproductive function, although there were no differences in timing between CD38 KO and age-matched WT controls (Figure 5B). There was a prominent age-dependent decline in the number of litters produced per dam irrespective of genotype (Figure 5C). At each time point, there was no difference in the number of litters produced per dam when comparing CD38 KO females to WT controls.

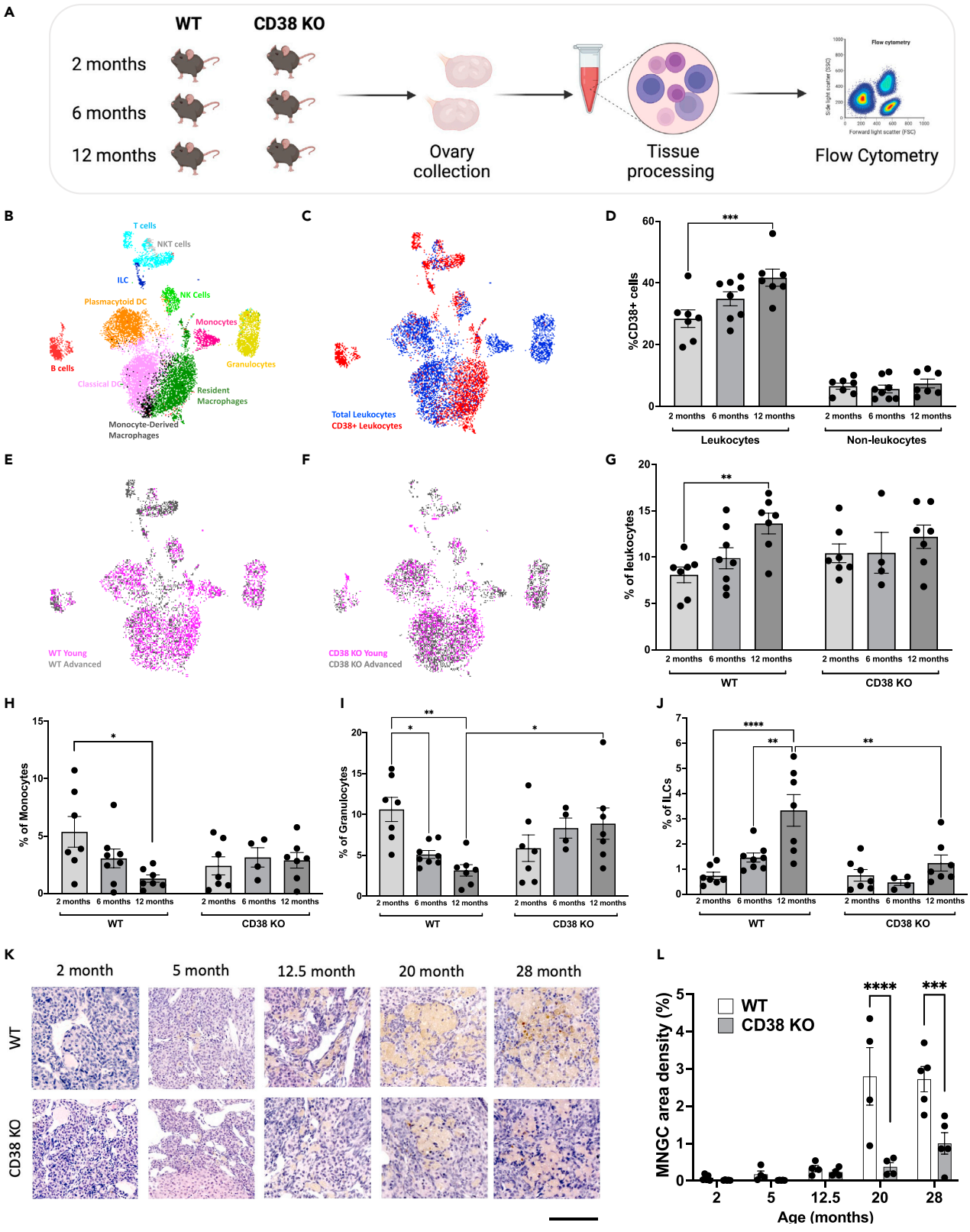
A
WT
CD38 KO
2 months
6 months
12 months
Ovary collection
Tissue processing
Flow Cytometry
B
T cells
NKT cells
ILC
NK Cells
Plasmacytoid DC
Monocytes
Granulocytes
B cells
Classical DC
Resident Macrophages
Monocyte-Derived Macrophages
C
Total Leukocytes
CD38+ Leukocytes
D
%CD38+ cells
Leukocytes
Non-leukocytes
E
WT Young
WT Advanced
F
CD38 KO Young
CD38 KO Advanced
G
% of leukocytes
WT
CD38 KO
H
% of Monocytes
I
% of Granulocytes
J
% of ILCs
K
2 month
5 month
12.5 month
20 month
28 month
WT
CD38 KO
L
MNGC area density (%)
WT
CD38 KO
Age (months)

Figure 3. CD38 expressing ovarian immune cells increase with age and CD38 KO animals are partially protected from age-associated ovarian immune changes

(A) Schematic of flow cytometry-based ovarian immunophenotypic analysis of 2, 6, and 12 month old females.

(B) UMAP plot featuring the different immune cell subclusters belonging to the murine ovarian immune landscape (C) UMAP plot featuring CD38 expressing immune cells within the WT ovarian immune landscape (D) Percentage of CD38 positive ($CD38^+$) cells within the ovarian WT leukocytes ($CD45^+$) and non-leukocytes ($CD45^-$) population throughout reproductive aging (n = 7–8 per group, mean ± SEM, two-way ANOVA statistical analysis *** = $p < 0.0005$).

(E and F) UMAP plot featuring immune cells distribution within the young and old (E) WT and (F) CD38 KO ovarian immune landscape.

(G–J) Percentage of total (G) leukocytes ($CD45^+$), (H) Monocytes (CD11b+, F4/80-, Ly6C+, Ly6G-), (I) Granulocytes (CD11b+, F4/80-, Ly6C+, Ly6G+) and (J) ILCs ($CD3^-$, $CD19^-$, CD138-, NK1.1-, CD11b-, CD127+) throughout murine reproductive aging in WT and CD38 KO ovaries (n = 4–8 per group, mean ± SEM, two-way ANOVA statistical analysis * = $p < 0.05$, ** = $p < 0.005$, **** = $p < 0.00005$).

(K) Representative images of H&E stained ovarian sections from 2, 5, 12.5, 20, and 28 month old WT and CD38 KO mice visualized by bright-field microscopy, 100 μm scale.

(L) Quantification of MNGCs density in ovarian sections from 2, 5, 12.5, 20, and 28 month old WT and CD38 KO females (n = 4–5 per group, mean ± SEM, two-way ANOVA statistical analysis *** = $p = 0.0002$, **** = $p < 0.0001$). All data are represented as mean ± SEM. See also Figure S2.

Interestingly, although the number of litters per breeder was similar between CD38 KO animals and WT controls, the reproductively young CD38 KO females produced a significantly larger number of pups per litter during the breeding trial period (Figure 5D) and showed overall a larger number of pups per dam (Figure 5E). In our study, no differences in pup survival were observed before weaning between the WT and CD38 KO genotypes in any of the age groups (Figure S3A). These findings are consistent with another study demonstrating that oxytocin-related impairments were much milder in CD38 KO pups suggesting the existence of a critical time window of CD38-mediated oxytocin regulation.[38] Overall, these data demonstrate that the increased number of follicles observed in reproductively young CD38 KO females is associated with enhanced fecundity. However, just as the increased follicle number is not sustained during aging, neither is the increase in total number of pups per dam (Figure 5E).

Increased ovarian NAD+ is associated with enhanced fecundity

CD38 regulates ovarian NAD+ consumption, and NAD+ is important for reproductive function.[13] Thus, we anticipated that the enhanced reproductive function both in terms of follicle number and fecundity in CD38 KO mice may be due to increased NAD+ levels. Thus, ovaries of the female dams were collected at the end of the breeding trial and analyzed for NAD+ content via mass spectrometry. NAD+ levels were significantly higher in ovaries from CD38 KO mice compared to WT controls at the reproductively young time point, although no differences between genotypes were observed at the older time points (Figure 5F). These data demonstrate that loss of CD38 in reproductively young females results in increased ovarian NAD+ levels which likely underlies improved reproductive outcomes. We also examined whether there was a correlation between ovarian NAD+ levels in the three breeding groups and their corresponding total litters per dam and total pups per litter (Figures S3B and S3C). There was a subtle but significant correlation between CD38KO ovarian NAD+ and the total litters per dam (Figure S3B) suggesting that higher ovarian NAD+ is potentially associated with increased litter numbers. No correlation was observed between NAD+ levels and total pups per dam in both genotypes (Figure S3C). Interestingly, the reproductively advanced age group of both genotypes had very low NAD+ levels that correlated with their reduced reproductive potential.

Neonatal ovaries from CD38 KO mice reveals a delayed establishment of the ovarian reserve

To further investigate why reproductively young CD38 KO mice have a larger number of primordial follicles, we investigated neonatal stages of ovarian development when the ovarian reserve is established. Female mice and humans are born with a fixed number of primordial follicles, also known as the ovarian reserve, which intrinsically determines the timeline of female reproductive longevity and fertility by virtue of the size of the initial follicular reserve and the rate of follicular death or maturation.[39] The initial formation of the ovarian reserve is a complex embryonic developmental process and it occurs during the early stages of oogenesis which involves germ cell cyst formation, organelle donation, and eventual cyst breakdown to form the primordial follicle reserve.[40] The timeline for mouse oogenesis differs between genetic mouse strains, but the C57BL6J strain undergoes complete cyst breakdown by postnatal-day-two (P2).[41] CD38 protein is expressed in P2 ovaries, and its localization was completely extrafollicular, similar to what we observed in adult ovaries (Figure 6A and 6A′). As expected, there was no CD38 expression in P2 ovaries from CD38 KO mice (Figure 6B).

When comparing the histology of P2 ovaries from CD38 KO and WT mice, we observed strikingly different morphology between genotypes (Figures 6C and 6D). Whereas ovaries from WT mice exhibited individualized primordial and primary follicles, ovaries from CD38 KO mice had fewer fully formed primordial follicles and contained many small clusters that stained darkly with hematoxylin in the central region of the ovary (Figures 6C and 6D).

To further characterize P2 ovaries from both WT and CD38 KO mice, we performed immunohistochemistry with the germ cell marker DDX4 (DEAD-Box Helicase 4, also known as VASA), a broad marker for germ cells from early embryonic development until they form antral follicles in adult ovaries.[42,43] We observed that ovaries from WT mice had larger DDX4 positive oocytes in the central medullary region of the ovary (Figure 6E) while oocytes in CD38 KO mouse ovaries tended to be smaller and confined to the outer cortex (Figure 6F). We confirmed this observation via immunofluorescence staining for both DDX4 and TRA98 (germ cell-specific antigen, also known as GCNA1) (Figures 6G and 6H). TRA98, like DDX4, is first expressed in germ cells during early embryonic development, but TRA98 expression is lost from oocytes in the

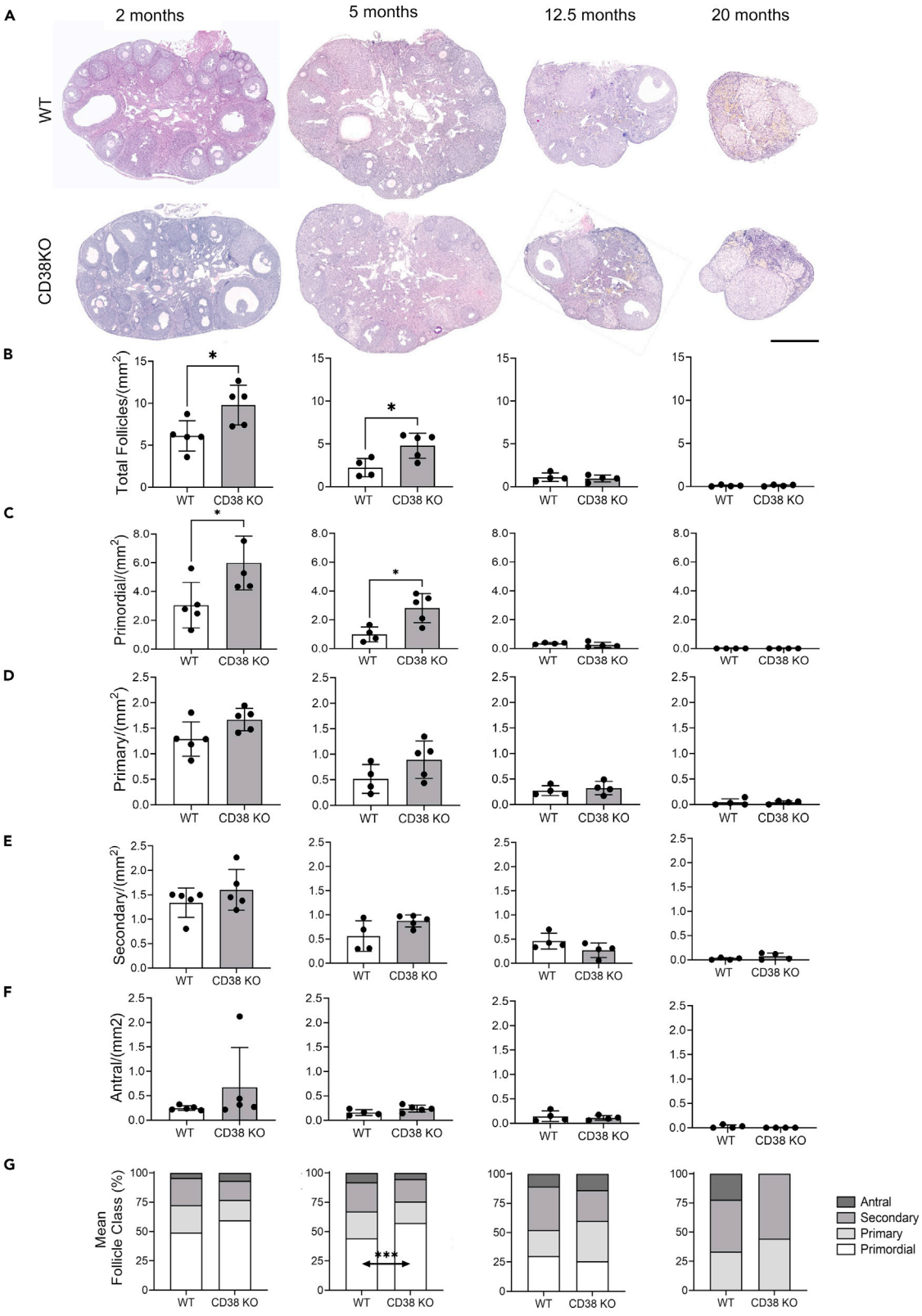
A
2 months
5 months
12.5 months
20 months
WT
CD38KO
B
Total Follicles/(mm2)
C
Primordial/(mm2)
D
Primary/(mm2)
E
Secondary/(mm2)
F
Antral/(mm2)
G
Mean Follicle Class (%)
WT
CD38 KO
Antral
Secondary
Primary
Primordial

Figure 4. Reproductively young CD38 KO female mice have a larger ovarian reserve compared to age-matched WT

(A) Representative images of H&E stained ovarian sections from 2, 5, 12.5, and 20 months old WT and CD38 KO mice visualized by bright-field microscopy, 500 μm scale.

(B) Total follicle quantification in ovaries from 2, 5, 12.5, and 20 months old WT and CD38 KO mice (n = 4–5 per group).

(C–F) (C) Primordial, (D) primary, (E) secondary, (F) antral follicles quantification in ovaries from 2, 5, 12.5, and 20 months old WT and CD38 KO mice (n = 4–5 per group) (Paired t-test statistical analysis *p < 0.05). All data are represented as mean ± SEM.

(G) Follicle classes detected as a percentage of the total ovarian follicle pool in ovaries from 2, 5, 12.5, and 20 months old WT and CD38 KO mice. (two-way ANOVA statistical analysis ***p < 0.0005).

medulla of the postnatal ovary when they arrest at the dictate stage and form primordial follicles.[44] Quantification of TRA98+ and DDX4+ oocytes revealed that there was an increasing trend in TRA98+ germ cells and significantly more DDX4+ germ cells in ovaries from CD38 KO mice relative to age-matched controls (Figures 6I and 6J). Moreover, there were differences in the size and distribution of the germ cells between the two genotypes. The average diameter of DDX4+ oocytes from WT mice were larger than those from CD38 KO mice (Figures 6G′, 6H′, and 6K). These larger oocytes in ovaries from WT mice were part of more advanced stage follicles that were developing in the central medullary region of the ovary (Figures 6C, 6E, and 6G). In contrast, the smaller oocytes in ovaries from CD38 KO mice tended to be confined to the outer cortex (Figures 6D, 6F, and 6H). Overall, our analysis revealed that ovaries from WT mice had an increased number of more advanced stage oocytes at P2 relative to CD38 KO mice. These data suggest that CD38 KO mice may have an extended window of follicle formation during early development which may enable the endowment of a larger ovarian reserve.

DISCUSSION

The ovary is the first organ to age contributing to infertility and loss of endocrine function. NAD+ metabolism is involved in energy metabolism, DNA repair, and redox signaling, and NAD+ decline in whole ovarian tissue and oocytes occurs with advanced reproductive age.[8,10,11] Supplementation of reproductively old mice with NAD+ precursors increases ovarian NAD+ levels and rescues fertility.[10] Furthermore, NAD+-dependent proteins such as sirtuins have beneficial effects in preserving ovarian reserve and reversing ovarian aging in reproductively old mice.[10,45–47] Despite the importance of NAD+ metabolism in ovarian aging, the underlying mechanisms driving NAD+ decline have been elusive. In this study, we showed that the NADase CD38 contributes to ovarian NAD+ decline, and that CD38 deficiency improves ovarian function early in the reproductive lifespan.

CD38 is a major NAD+-consuming enzyme in several aging tissues, including the liver, adipose, spleen, and skeletal muscle, with overall elevated CD38 expression observed at advanced chronologic age (24–32 months).[20,26] Interestingly, we observed an age-dependent increase in CD38 in the ovary, coincident with an increase in NADase activity by 12 months, which represents a reproductive aging time point. Thus, our data suggest that increased CD38 levels are a hallmark of general tissue-specific aging irrespective of the chronological time frame.

CD38 degrades NAD+ to produce NAM and ADPR through its hydrolase activity, and cyclic ADPR (cADPR) via its cyclase activity, and our results demonstrate that CD38 actively regulates ovarian NAD+ metabolism.[48] Ovaries from CD38 KO animals exhibited an increase in NAD+ levels and a decrease in NAM and ADPR levels. Under normal physiological circumstances, NAM is constantly recycled to form NAD+ through the salvage pathway. Indeed, ovarian NAM levels correlated with NAD+ levels, and the absence of NAM accumulation indicated active biosynthesis through the salvage pathway. Moreover, at 20 months of age, when NAD+ levels in the CD38 KO ovaries were similar to WT levels, NAM levels also returned to WT levels. In contrast to NAM, ADPR levels were strongly suppressed across reproductive ages, and this suppression was still prominent at 20 months of age in CD38 KO ovaries. We speculate that ADPR, being a secondary messenger that mobilizes Ca^{2+} ions, was consistently used at all time points, and the observation that ADPR levels did not decrease further suggested that its levels were sufficient. We also predict that cADPR, another secondary messenger produced by CD38's cyclase activity, would behave similarly to ADPR, but due to its low abundance, we could not robustly measure this metabolite.

Although CD38 has been implicated as an immune cell marker in the context of ovarian cancer, its role in ovarian physiology and aging has not been elucidated.[49–51] CD38 expression was enriched in extrafollicular ovarian compartments such as the stroma, vasculature, and CLs, with minimal to no expression within follicles at any stage of development. Our analysis revealed an age-associated decreasing trend in NAD+ levels, although not significant, in whole ovaries which include both follicles and extrafollicular structures. Bertoldo et al.[10] also found no significant decrease in NAD+ between 2 and 14 months old female whole ovaries. Previous reports have demonstrated that NAD+ levels decline within oocytes during reproductive aging in mice and that biochemical processes in the cumulus cells can affect the redox status of oocytes *in vitro*.[52] Because CD38 is not expressed in the follicle, it is possible that other yet-to-be-identified factors may underlie the age-dependent decline of NAD+ in oocytes. Alternatively, there may be an indirect effect given the sophisticated system of communication and signaling between cells of the follicle—including oocytes, granulosa cells, and theca cells—and cells of the surrounding stromal tissue, such as fibroblasts, endothelial cells, and immune cells.[29]

Although CD38 is expressed in several cell populations, it is predominantly expressed in ovarian immune cells, consistent with high CD38 expression in immune cells in other tissues.[23,32,53] The localization of CD38 positive cells within the stroma and the CLs also confirms cellular identity given that these structures are enriched in leukocytes and are sites of immune infiltration and inflammation.[29,54] Within the ovary, immune cells are localized throughout the stroma and around the theca vasculature and play a key role in physiological ovarian processes such as ovulation. In the CLs, immune cell infiltration is essential for postovulatory events such as CL regression.[54] Our immunophenotypic analysis revealed that CD38 is highly expressed in populations of both the innate and adaptive ovarian immune landscape, including B cells, T cells, macrophages, NK, NKT, and ILCs. Resident macrophages and DC represent the most abundant immune cell type in the ovary irrespective of

A

WT x WT		WT x CD38 KO	
WT Male	WT Female	WT Male	CD38 KO Female
3 months	2 months	3 months	2 months
3 months	6 months	3 months	6 months
3 months	12 months	3 months	12 months

6 months 1:1 cohabitation

Pups per dam and per litter

Total litters per dam

Post-breeding trial dam ovarian NAD+ measurement

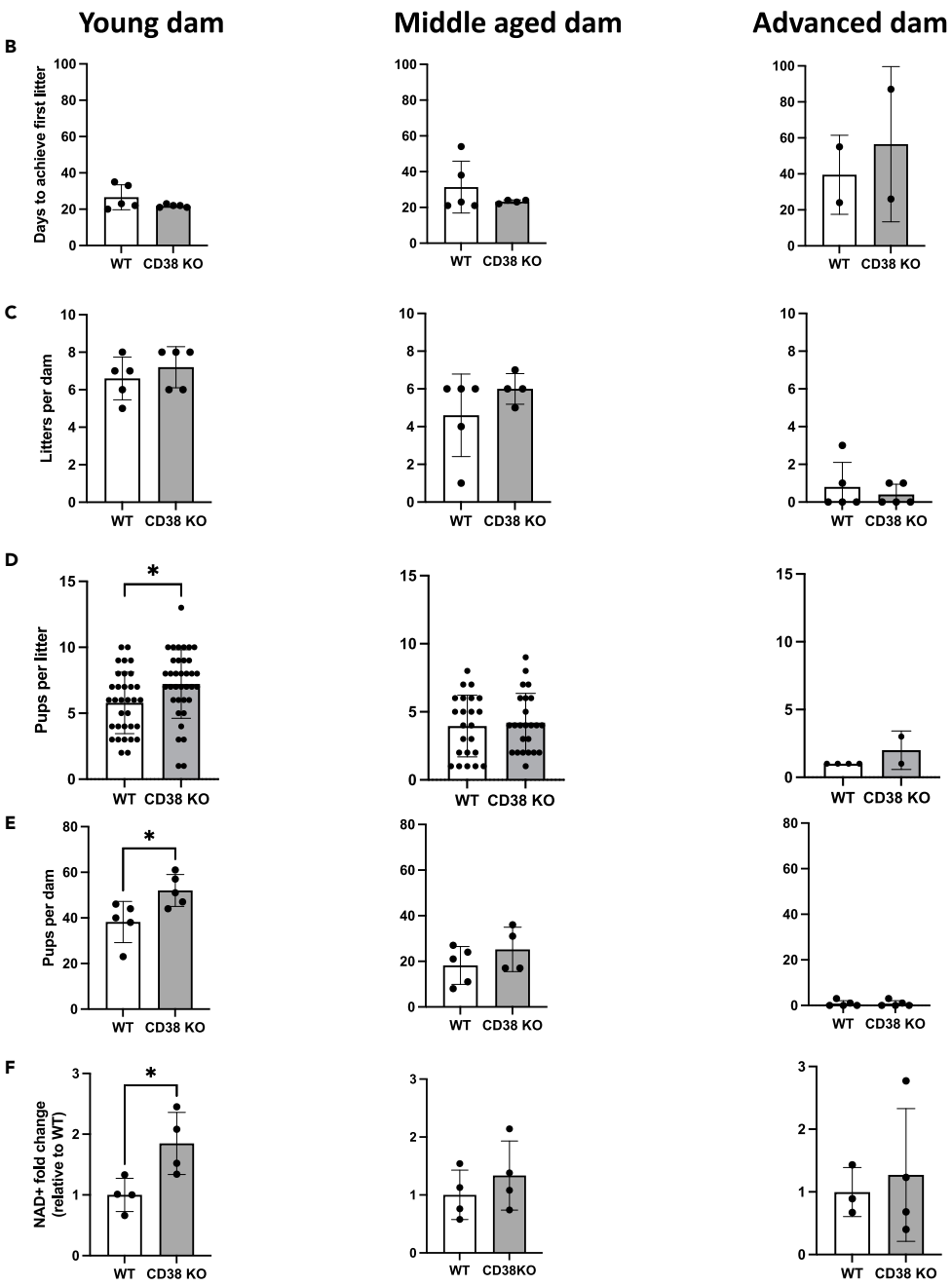

Figure 5. Reproductively young CD38 KO female mice generate more pups and have higher ovarian NAD+ levels compared to age-matched WT

(A) Breeding schematic of 6-month breeding trial crossing 2 (young), 6 (middle-aged), 12 months (advanced) old WT and CD38 KO females with 3 months old WT males.

(B and C) (B) Number of days to generate their first litter and (C) total number of litters for each dam in the 3 different female age groups (young, middle-aged, and advanced) throughout the 6-month breeding trial.

(D and E) (D) Total number of pups per litter and (E) total numbers of pups per dam generated by the 3 different female age groups (young, middle-aged, and advanced) throughout the 6-month breeding trial. (Unpaired t-test statistical analysis *$p < 0.05$).

(F) NAD+ levels of ovarian tissues collected from each female dam that survived the end of 6-month breeding trial (n = 3–4 per group, Mann Whitney test statistical analysis * = $p < 0.05$). All data are represented as mean ± SD. See also Figure S3.

age. Ovarian macrophages mostly localize in the stroma, CLs, and atretic follicles contributing to CLs regression and tissue homeostasis.[24] Macrophages also associate with growing follicles, promoting development and survival.[55] The most represented subpopulation of T cells was the DN population, characterized by expression of the alpha-beta T-cell receptor (TCR), but not the CD4 nor the CD8 co-receptors. The frequency of this subpopulation is usually very low in peripheral blood and tissues and emerging evidence suggests a key role in pathophysiological processes associated with autoimmunity and inflammation.[56]

Ovarian immune cell composition varies across the reproductive cycle and with age.[25,27] Our analysis confirmed that reproductive aging impacts the ovarian immune cell landscape with a decrease in macrophages and granulocytes and an increase in ILCs and T cells, mostly DN T cells. Similar trends in WT mouse ovaries were previously observed.[27,33] The decrease in innate immune cells, in particular macrophages, reflects the age-associated decrease in ovulation and wound healing and associated inflammation.[57]

Although ovaries from CD38 KO mice have an overall similar immune composition relative to WT controls, they did exhibit unique age-related immune trends. For instance, whereas ovaries from WT mice demonstrated an age-dependent decrease in granulocytes and an increase in ILCs, no differences was observed in the absence of CD38, suggesting a protective effect. In addition, ovaries from 12 month old CD38 KO mice showed increased granulocytes and decreased ILCs compared to age-matched WT counterparts. A hallmark of the aging ovary is accumulation of an unique population of multinucleated macrophage giant cells (MNGCs) which are associated with chronic inflammation. Although no differences in the relative abundance of MNGCs was observed during reproductive lifespan, the absence of CD38 was associated with a decrease in ovarian MNGCs at post-fertile ages (20 and 28 months), suggesting a decreased inflammatory milieu. Our data suggest an immuno-modulatory role in the absence of CD38, with only modest changes in fertile ages and potential protective effects in post-fertile ages. This observation is particularly relevant given that ovarian aging, as a result of continuous follicle atresia and clearance as well as repeated cycles of ovulation-associated inflammation, wound repair and remodeling, is associated with increased ovarian inflammation, fibrosis, and stiffness.[35,58–60] This microenvironment has potential ramifications for pathologies such as ovarian cancer.[61–63] To our knowledge, this is the first report showing the effect of CD38 genetic ablation in shaping the immune landscape during aging.

Genetic ablation of CD38 enhanced reproductive function in young females. CD38 KO animals had more primordial follicles than wild type counterparts at 2 and 5 months of age. This increased ovarian reserve was associated with increased fecundity and ovarian NAD+. Previous reports have linked improved fertility to restoration of ovarian NAD+ levels, albeit in reproductively aged females.[10,11] The beneficial effect of NAD+ in ovaries can be explained by regulation of sirtuins, which depend on NAD+. For example, ovarian SIRT1 prevents follicular activation and loss, influencing key cellular processes such as autophagy and mTOR -related metabolic pathways.[45,46,64] Interestingly, treatment with a SIRT1 agonist improves ovarian function in a mouse model of premature ovarian insufficiency (POI).[65] Moreover, overexpression of SIRT2 improves fertility and recapitulates the benefits of NMN supplementation.[10] SIRT3 is a mitochondrial sirtuin and its ovarian expression decreases with age leading to mitochondrial dysfunction and deleterious spindle assembly.[66]

One caveat of our study is that the CD38 KO and WT females were not from the same litter. Use of separate colonies to generate these genotypes might have influenced early life environmental factors with potential repercussions on future reproductive outcomes. However, the phenotypes we observed correlated well with distinct changes in NAD+ metabolism which are expected with CD38 loss-of-function (Figure 2). Furthermore, our data are consistent with previously published studies showing a positive correlation between increased NAD+ levels and fertility suggesting the contribution of CD38 to this phenomenon.[10,11] Nevertheless, future studies using matched WT and CD38 KO females from the same litter will provide further validation of our findings. In addition, we cannot exclude the potential systemic influence of CD38 deficiency on the reproductive capacity and ovarian function. In fact, CD38 is ubiquitously expressed throughout the mouse where it regulates key metabolic processes such as glucose tolerance and insulin sensitivity[26,67] which can greatly influence the reproductive system.[68,69] In addition, CD38 has been previously shown to influence hormonal regulation, such as oxytocin release,[70] and to be regulated by steroid hormones estrogen and progesterone.[71] It remains unclear whether targeting CD38 to improve female fertility could lead to effects other than increasing NAD+, such as impacting oxytocin release as previously described in rodents.[37] Interestingly, recent evidence suggests a potential advantage of oxytocin antagonists for assisted reproduction.[72,73] The systemic contribution of CD38 loss remains an important area to investigate in future studies and underscores the need to further employ tissue- and cell-specific CD38 KO systems. Nevertheless, our data suggest a role of CD38 in the establishment of the ovarian reserve which is considered a gonadotropin independent process.[74]

Our data reveal an unexpected and novel role for CD38 in early follicle development. Ovaries from CD38 KO mice showed a prolonged period of follicle formation which likely underlies the larger ovarian reserve until young adulthood. At postnatal day 2, ovaries from CD38 KO mice had a larger number of germ cells that were in an earlier stage of development as evidenced by their smaller size relative to WT controls. Both extrinsic and intrinsic factors can contribute to the timeline of cyst breakdown and follicle formation during oogenesis, including

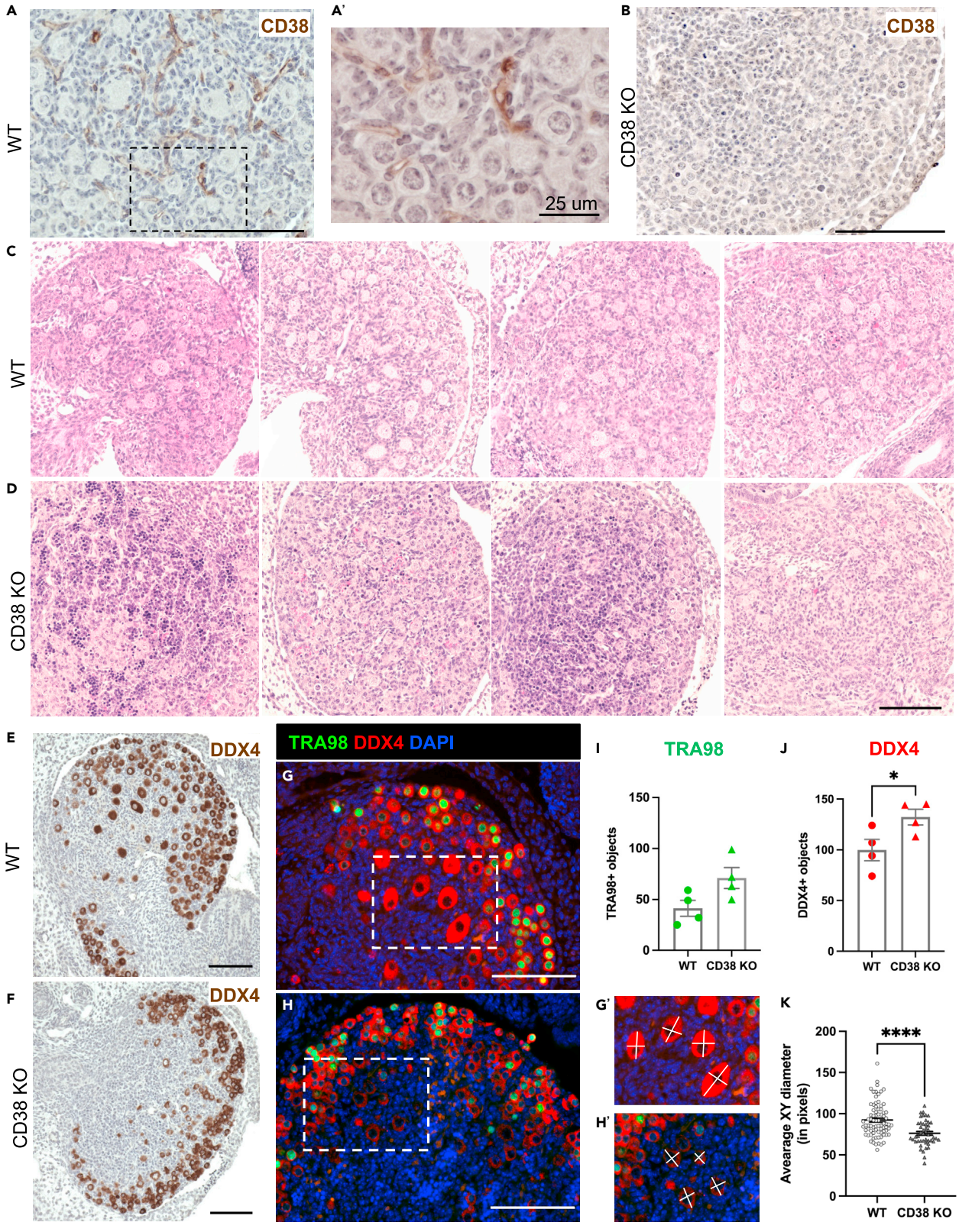
A
CD38
WT
A'
25 um
B
CD38
CD38 KO
C
WT
D
CD38 KO
E
DDX4
WT
F
DDX4
CD38 KO
TRA98 DDX4 DAPI
G
H
I
TRA98
TRA98+ objects
150
100
50
0
WT
CD38 KO
J
DDX4
*
DDX4+ objects
150
100
50
0
WT
CD38 KO
G'
H'
K
****
Avearage XY diameter (in pixels)
200
150
100
50
0
WT
CD38 KO

Figure 6. Neonatal ovaries from CD38 KO mice have delayed establishment of the ovarian follicular reserve

(A) Representative immunohistochemistry image of postnatal day 2 mouse ovaries from WT animal stained with CD38 antibody, 100 μm scale.

(A′) Higher magnification image of 5A, 25 μm scale.

(B) Representative immunohistochemistry image of postnatal day 2 mouse ovaries from CD38 KO animal stained with CD38 antibody as a control, 100 μm scale.

(C and D) Representative images of H&E stained ovarian sections from postnatal day 2 (C) WT (n = 4) and (D) CD38 KO (n = 4) mice visualized by bright-field microscopy, 100 μm scale.

(E and F) Representative immunohistochemistry images of postnatal day 2 mouse ovaries from (E) WT and (F) CD38 KO animals stained with the germ cell marker DDX4 antibody, 100 μm scale.

(G and H) Representative immunofluorescent images of postnatal day 2 mouse ovaries stained with TRA98 (green) and DDX4 (red) antibodies to label germ cells in (G) WT and (H) CD38 KO, 100 μm scale. Dashed rectangles in G and H show the borders of zoom in (G′) and (H′), respectively.

(I) Quantification of TRA98 positive germ cells in WT and CD38 KO postnatal day 2 ovaries (n = 4 for each genotype) (Unpaired t-test statistical analysis p = 0.0614).

(J) Quantification of DDX4 positive germ cells in WT and CD38 KO postnatal day 2 ovaries (n = 4 for each genotype) (Unpaired t-test statistical analysis * = $p < 0.05$). The white lines in (G′) and (H′) show examples of measurements for calculating the average XY diameter of DDX4+ germ cells.

(K) Average XY diameter of DDX4+ germ cells in the medullary region of WT and CD38 KO postnatal day 2 ovaries (n = 64 and n = 41) DDX4+ cells analyzed from total of four WT and CD38 KO ovary sections, respectively (Unpaired t-test statistical analysis ****$p < 0.0001$). All data are represented as mean ± SEM.

starvation, exposure to endocrine disruptors and hormones, as well as genetic regulators.[75,76] Future studies are warranted to determine CD38-driven mechanisms regulating follicle formation.

The positive effects of CD38 deficiency on ovarian function were not sustained with age, and this may be due to several reasons. First, there could be a detrimental effect of CD38 deficiency in immune response with progressive aging. CD38 is necessary for immune cell infiltration and cell signaling, and the whole-body CD38 KO may have broader immunomodulatory effects not captured through our analysis which focused on composition rather than function. Lack of CD38 impacts immune response to infections, resulting in lower innate immune infiltration and neutrophil number.[53] Second, compensatory metabolic mechanisms in the total body CD38 KO model could override the beneficial effect of CD38 deficiency later in reproductive life. Since this phenotype can potentially be associated with the systemic lack of CD38 in the total body knockout mice, further studies with selective CD38 small molecule inhibitors or conditional knockout animal models will be informative.

Overall, our findings demonstrate that CD38 loss-of-function early in the reproductive lifespan increased NAD+ levels and improved ovarian function. However, this beneficial effect is not sustained during reproductive aging. Further studies are needed to fully understand the mechanisms underlying the CD38-NAD+ axis in the ovary in the context of age-related ovarian dysfunction. Furthermore, impaired ovarian NAD+ metabolism has been linked to various ovarian dysfunctions such as infertility, premature ovarian failure, and polycystic ovarian syndrome.[4,10,77] Thus, understanding the role of CD38 in ovarian NAD+ metabolism has the potential to lead to novel therapeutic interventions for reproductive health and longevity.

Limitations of the study

In this study, the use of a total body CD38 KO model may be associated to systemic effects arising from the absence of CD38. To gain deeper insights on the role of CD38 on ovarian function, it is imperative to design future studies utilizing animal models that feature tissue and cell-specific conditional knockouts. Moreover, we acknowledge the possibility that maintaining the CD38 knockout allele as homozygotes with separate breeding colonies could have influenced early life environmental factors with potential repercussions for future reproductive outcomes. Additional research employing WT and CD38 KO littermates are required to validate our observations.

In addition, since intracellular NAD+ levels are intricately regulated by both NAD+ consumption and biosynthetic pathways, we cannot exclude potential contributions of other NAD+-related enzymes such as PARP and Sirtuins on the observed phenotype. Future studies including evaluation of other NAD+ consuming and generating enzymes will provide a more comprehensive understanding of the phenomenon.

STAR★METHODS

Detailed methods are provided in the online version of this paper and include the following:

- KEY RESOURCES TABLE
- RESOURCE AVAILABILITY
  - Lead contact
  - Materials availability
  - Data and code availability
- EXPERIMENTAL MODEL AND STUDY PARTICIPANT DETAILS
  - Animals
- METHOD DETAILS
  - Ovarian tissue fixation, processing, and embedding
  - RNA *in situ* hybridization and transcript quantification
  - Colorimetric immunohistochemistry (IHC)

- Immunofluorescence
- Immunoblot analysis
- In-silico analysis of publicly available ovarian bulk RNAseq data
- Whole ovary tissue hydrolase activity assay
- LCMS analysis of the ovary
- Flow cytometry
- MNGC quantification
- Follicle classification and counting
- Breeding trial
- Hematoxylin and eosin staining

● QUANTIFICATION AND STATISTICAL ANALYSIS

SUPPLEMENTAL INFORMATION

Supplemental information can be found online at https://doi.org/10.1016/j.isci.2023.107949.

ACKNOWLEDGMENTS

We thank Dr. Elena Silva, Kaitlyn Vitangcol, Stella Breslin, and Harris Ingle for technical assistance and useful discussion. This study was supported by the Bia-Echo Foundation, the Sergey Brin Family Foundation and the Buck Institute For Research on Aging Institutional fundings.

AUTHOR CONTRIBUTIONS

Conceptualization, R.P., P.V.A.K., L.H., F.E.D., E.V.; Methodology, P.V.A.K., L.H., C.H, J.B., B.S.K., K.H.; Formal analysis, R.P., P.V.A.K., L.H., C.H, B.S.K., K.H., H.M., I.H., M.S-K.; Investigation, P.V.A.K., L.H., C.H, R.R., G.Z., B.S.K., K.H., L.P., R.T., G.V.H., ; Writing—original draft preparation, R.P., P.V.A.K., L.H., C.H., Writing—review and editing, R.P., P.V.A.K., F.E.D.; Supervision, R.P., F.E.D., E.V.; Funding acquisition, E.V. All authors have read and agreed to the published version of the manuscript.

DECLARATION OF INTERESTS

E.V. is a scientific co-founder, shareholder and advisors of Napa Therapeutics, Ltd. E.V., R.P. and P.V.A.K. receive research support from Napa Therapeutics, Ltd.

INCLUSION AND DIVERSITY

We support inclusive, diverse, and equitable conduct of research.

Received: April 18, 2023
Revised: May 24, 2023
Accepted: September 14, 2023
Published: September 16, 2023

REFERENCES

1. Hall, J.E. (2015). Endocrinology of the Menopause. Endocrinol Metab. Clin. N. Am. *44*, 485–496.
2. Torre, S.D., Benedusi, V., Fontana, R., and Maggi, A. (2013). Energy metabolism and fertility—a balance preserved for female health. Nat. Rev. Endocrinol. *10*, 13–23.
3. Katsyuba, E., Romani, M., Hofer, D., and Auwerx, J. (2020). NAD+ homeostasis in health and disease. Nat. Metab. *2*, 9–31.
4. Wang, Y., Yang, Q., Wang, H., Zhu, J., Cong, L., Li, H., and Sun, Y. (2021). NAD+ deficiency and mitochondrial dysfunction in granulosa cells of women with polycystic ovary syndrome. Biol. Reprod. *105*, 371–380.
5. Sirotkin, A.V. (2016). The Role and Application of Sirtuins and mTOR Signaling in the Control of Ovarian Functions. Cells *5*. https://doi.org/10.3390/cells5040042.
6. Ruszkiewicz, J.A., Bürkle, A., and Mangerich, A. (2022). Fueling genome maintenance: On the versatile roles of NAD+ in preserving DNA integrity. J. Biol. Chem. *298*, 102037.
7. Fang, E.F., Lautrup, S., Hou, Y., Demarest, T.G., Croteau, D.L., Mattson, M.P., and Bohr, V.A. (2017). NAD+ in Aging: Molecular Mechanisms and Translational Implications. Trends Mol. Med. *23*, 899–916.
8. Covarrubias, A.J., Perrone, R., Grozio, A., and Verdin, E. (2021). NAD+ metabolism and its roles in cellular processes during ageing. Nat. Rev. Mol. Cell Biol. *22*, 119–141.
9. McReynolds, M.R., Chellappa, K., and Baur, J.A. (2020). Age-related NAD+ decline. Exp. Gerontol. *134*, 110888.
10. Bertoldo, M.J., Listijono, D.R., Ho, W.-H.J., Riepsamen, A.H., Goss, D.M., Richani, D., Jin, X.L., Mahbub, S., Campbell, J.M., Habibalahi, A., et al. (2020). NAD Repletion Rescues Female Fertility during Reproductive Aging. Cell Rep. *30*, 1670–1681.e7.
11. Yang, Q., Cong, L., Wang, Y., Luo, X., Li, H., Wang, H., Zhu, J., Dai, S., Jin, H., Yao, G., et al. (2020). Increasing ovarian NAD levels improve mitochondrial functions and reverse ovarian aging. Free Radic. Biol. Med. *156*, 1–10.
12. Miao, Y., Cui, Z., Gao, Q., Rui, R., and Xiong, B. (2020). Nicotinamide Mononucleotide Supplementation Reverses the Declining Quality of Maternally Aged Oocytes. Cell Rep. *32*, 107987.
13. Huang, P., Zhou, Y., Tang, W., Ren, C., Jiang, A., Wang, X., Qian, X., Zhou, Z., and Gong, A. (2022). Long-term treatment of Nicotinamide mononucleotide improved age-related diminished ovary reserve through enhancing the mitophagy level of granulosa cells in mice. J. Nutr. Biochem. *101*, 108911.
14. Schultz, M.B., and Sinclair, D.A. (2016). Why NAD(+) Declines during Aging: It's Destroyed. Cell Metabol. *23*, 965–966.
15. Aksoy, P., White, T.A., Thompson, M., and Chini, E.N. (2006). Regulation of intracellular levels of NAD: a novel role for CD38. Biochem. Biophys. Res. Commun. *345*, 1386–1392.

16. Zeidler, J.D., Hogan, K.A., Agorrody, G., Peclat, T.R., Kashyap, S., Kanamori, K.S., Gomez, L.S., Mazdeh, D.Z., Warner, G.M., Thompson, K.L., et al. (2022). The CD38 glycohydrolase and the NAD sink: implications for pathological conditions. Am. J. Physiol. Cell Physiol. *322*, C521–C545.
17. Mehta, K., Shahid, U., and Malavasi, F. (1996). Human CD38, a cell-surface protein with multiple functions. FASEB J. *10*, 1408–1417.
18. Adebanjo, O.A., Anandatheerthavarada, H.K., Koval, A.P., Moonga, B.S., Biswas, G., Sun, L., Sodam, B.R., Bevis, P.J., Huang, C.L., Epstein, S., et al. (1999). A new function for CD38/ADP-ribosyl cyclase in nuclear Ca2+ homeostasis. Nat. Cell Biol. *1*, 409–414.
19. Chubanava, S., and Treebak, J.T. (2023). Regular exercise effectively protects against the aging-associated decline in skeletal muscle NAD content. Exp. Gerontol. *173*, 112109.
20. Tarragó, M.G., Chini, C.C.S., Kanamori, K.S., Warner, G.M., Caride, A., de Oliveira, G.C., Rud, M., Samani, A., Hein, K.Z., Huang, R., et al. (2018). A Potent and Specific CD38 Inhibitor Ameliorates Age-Related Metabolic Dysfunction by Reversing Tissue NAD Decline. Cell Metabol. *27*, 1081–1095.e10.
21. Chini, E.N., Chini, C.C.S., Espindola Netto, J.M., de Oliveira, G.C., and van Schooten, W. (2018). The Pharmacology of CD38/NADase: An Emerging Target in Cancer and Diseases of Aging. Trends Pharmacol. Sci. *39*, 424–436.
22. Covarrubias, A.J., Kale, A., Perrone, R., Lopez-Dominguez, J.A., Pisco, A.O., Kasler, H.G., Schmidt, M.S., Heckenbach, I., Kwok, R., Wiley, C.D., et al. (2020). Senescent cells promote tissue NAD decline during ageing via the activation of CD38 macrophages. Nat. Metab. *2*, 1265–1283.
23. Chini, C.C.S., Peclat, T.R., Warner, G.M., Kashyap, S., Espindola-Netto, J.M., de Oliveira, G.C., Gomez, L.S., Hogan, K.A., Tarragó, M.G., Puranik, A.S., et al. (2020). CD38 ecto-enzyme in immune cells is induced during aging and regulates NAD and NMN levels. Nat. Metab. *2*, 1284–1304.
24. Zhang, Z., Huang, L., and Brayboy, L. (2021). Macrophages: an indispensable piece of ovarian health. Biol. Reprod. *104*, 527–538.
25. Morris, M.E., Meinsohn, M.-C., Chauvin, M., Saatcioglu, H.D., Kashiwagi, A., Sicher, N.A., Nguyen, N., Yuan, S., Stavely, R., Hyun, M., et al. (2022). A single-cell atlas of the cycling murine ovary. Elife *11*, e77239. https://doi.org/10.7554/eLife.77239.
26. Camacho-Pereira, J., Tarragó, M.G., Chini, C.C.S., Nin, V., Escande, C., Warner, G.M., Puranik, A.S., Schoon, R.A., Reid, J.M., Galina, A., and Chini, E.N. (2016). CD38 Dictates Age-Related NAD Decline and Mitochondrial Dysfunction through an SIRT3-Dependent Mechanism. Cell Metabol. *23*, 1127–1139.
27. Zhang, Z., Schlamp, F., Huang, L., Clark, H., and Brayboy, L. (2020). Inflammaging is associated with shifted macrophage ontogeny and polarization in the aging mouse ovary. Reproduction *159*, 325–337.
28. de Oliveira, G.C., Kanamori, K.S., Auxiliadora-Martins, M., Chini, C.C.S., and Chini, E.N. (2018). Measuring CD38 Hydrolase and Cyclase Activities: 1,N-Ethenonicotinamide Adenine Dinucleotide (ε-NAD) and Nicotinamide Guanine Dinucleotide (NGD) Fluorescence-based Methods. Bio. Protoc. *8*, e2938. https://doi.org/10.21769/BioProtoc.2938.
29. Kinnear, H.M., Tomaszewski, C.E., Chang, F.L., Moravek, M.B., Xu, M., Padmanabhan, V., and Shikanov, A. (2020). The ovarian stroma as a new frontier. Reproduction *160*, R25–R39.
30. Han, X., Wang, R., Zhou, Y., Fei, L., Sun, H., Lai, S., Saadatpour, A., Zhou, Z., Chen, H., Ye, F., et al. (2018). Mapping the Mouse Cell Atlas by Microwell-Seq. Cell *172*, 1091–1107.e17.
31. Field, S.L., Dasgupta, T., Cummings, M., and Orsi, N.M. (2014). Cytokines in ovarian folliculogenesis, oocyte maturation and luteinisation. Mol. Reprod. Dev. *81*, 284–314.
32. Piedra-Quintero, Z.L., Wilson, Z., Nava, P., and Guerau-de-Arellano, M. (2020). CD38: An Immunomodulatory Molecule in Inflammation and Autoimmunity. Front. Immunol. *11*, 597959.
33. Landry, D.A., Yakubovich, E., Cook, D.P., Fasih, S., Upham, J., and Vanderhyden, B.C. (2022). Metformin prevents age-associated ovarian fibrosis by modulating the immune landscape in female mice. Sci. Adv. *8*, eabq1475.
34. Foley, K.G., Pritchard, M.T., and Duncan, F.E. (2021). Macrophage-derived multinucleated giant cells: hallmarks of the aging ovary. Reproduction *161*, V5–V9.
35. Briley, S.M., Jasti, S., McCracken, J.M., Hornick, J.E., Fegley, B., Pritchard, M.T., and Duncan, F.E. (2016). Reproductive age-associated fibrosis in the stroma of the mammalian ovary. Reproduction *152*, 245–260.
36. Duncan, F.E., Jasti, S., Paulson, A., Kelsh, J.M., Fegley, B., and Gerton, J.L. (2017). Age-associated dysregulation of protein metabolism in the mammalian oocyte. Aging Cell *16*, 1381–1393.
37. Jin, D., Liu, H.-X., Hirai, H., Torashima, T., Nagai, T., Lopatina, O., Shnayder, N.A., Yamada, K., Noda, M., Seike, T., et al. (2007). CD38 is critical for social behaviour by regulating oxytocin secretion. Nature *446*, 41–45.
38. Higashida, H., Lopatina, O., Yoshihara, T., Pichugina, Y.A., Soumarokov, A.A., Munesue, T., Minabe, Y., Kikuchi, M., Ono, Y., Korshunova, N., and Salmina, A.B. (2010). Oxytocin signal and social behaviour: comparison among adult and infant oxytocin, oxytocin receptor and CD38 gene knockout mice. J. Neuroendocrinol. *22*, 373–379.
39. Umeno, K., Sasaki, A., and Kimura, N. (2022). The impact of oocyte death on mouse primordial follicle formation and ovarian reserve. Reprod. Med. Biol. *21*, e12489.
40. Niu, W., and Spradling, A.C. (2022). Mouse oocytes develop in cysts with the help of nurse cells. Cell *185*, 2576–2590.e12.
41. Pepling, M.E., Sundman, E.A., Patterson, N.L., Gephardt, G.W., Medico, L., Jr., and Wilson, K.I. (2010). Differences in oocyte development and estradiol sensitivity among mouse strains. Reproduction *139*, 349–357.
42. Toyooka, Y., Tsunekawa, N., Takahashi, Y., Matsui, Y., Satoh, M., and Noce, T. (2000). Expression and intracellular localization of mouse Vasa-homologue protein during germ cell development. Mech. Dev. *93*, 139–149.
43. Song, K., Ma, W., Huang, C., Ding, J., Cui, D., and Zhang, M. (2016). Expression Pattern of Mouse Vasa Homologue (MVH) in the Ovaries of C57BL/6 Female Mice. Med. Sci. Mon. Int. Med. J. Exp. Clin. Res. *22*, 2656–2663.
44. Enders, G.C., and May, J.J., 2nd (1994). Developmentally regulated expression of a mouse germ cell nuclear antigen examined from embryonic day 11 to adult in male and female mice. Dev. Biol. *163*, 331–340.
45. Liu, W.-J., Zhang, X.-M., Wang, N., Zhou, X.-L., Fu, Y.-C., and Luo, L.-L. (2015). Calorie restriction inhibits ovarian follicle development and follicle loss through activating SIRT1 signaling in mice. Eur. J. Med. Res. *20*, 22.
46. Long, G.-Y., Yang, J.-Y., Xu, J.-J., Ni, Y.-H., Zhou, X.-L., Ma, J.-Y., Fu, Y.-C., and Luo, L.-L. (2019). SIRT1 knock-in mice preserve ovarian reserve resembling caloric restriction. Gene *686*, 194–202.
47. Zhou, X.-L., Xu, J.-J., Ni, Y.-H., Chen, X.-C., Zhang, H.-X., Zhang, X.-M., Liu, W.-J., Luo, L.-L., and Fu, Y.-C. (2014). SIRT1 activator (SRT1720) improves the follicle reserve and prolongs the ovarian lifespan of diet-induced obesity in female mice via activating SIRT1 and suppressing mTOR signaling. J. Ovarian Res. *7*, 97.
48. Lee, H.C. (2006). Structure and enzymatic functions of human CD38. Mol. Med. *12*, 317–323.
49. Zhou, J., Wang, W., Liang, Z., Ni, B., He, W., and Wang, D. (2020). Clinical significance of CD38 and CD101 expression in PD-1CD8 T cells in patients with epithelial ovarian cancer. Oncol. Lett. *20*, 724–732.
50. Zhu, Y., Zhang, Z., Jiang, Z., Liu, Y., and Zhou, J. (2020). CD38 Predicts Favorable Prognosis by Enhancing Immune Infiltration and Antitumor Immunity in the Epithelial Ovarian Cancer Microenvironment. Front. Genet. *11*, 369.
51. Wo, Y.J., Gan, A.S.P., Lim, X., Tay, I.S.Y., Lim, S., Lim, J.C.T., and Yeong, J.P.S. (2019). The Roles of CD38 and CD157 in the Solid Tumor Microenvironment and Cancer Immunotherapy. Cells *9*. https://doi.org/10.3390/cells9010026.
52. von Mengden, L., Klamt, F., and Smitz, J. (2020). Redox Biology of Human Cumulus Cells: Basic Concepts, Impact on Oocyte Quality, and Potential Clinical Use. Antioxidants Redox Signal. *32*, 522–535.
53. Glaría, E., and Valledor, A.F. (2020). Roles of CD38 in the Immune Response to Infection. Cells *9*. https://doi.org/10.3390/cells9010228.
54. Mlyczyńska, E., Kieżun, M., Kurowska, P., Dawid, M., Pich, K., Respekta, N., Daudon, M., Rytelewska, E., Dobrzyń, K., Kamińska, B., et al. (2022). New Aspects of Corpus Luteum Regulation in Physiological and Pathological Conditions: Involvement of Adipokines and Neuropeptides. Cells *11*. https://doi.org/10.3390/cells11060957.
55. Tingen, C.M., Kiesewetter, S.E., Jozefik, J., Thomas, C., Tagler, D., Shea, L., and Woodruff, T.K. (2011). A macrophage and theca cell-enriched stromal cell population influences growth and survival of immature murine follicles in vitro. Reproduction *141*, 809–820.
56. Velikkakam, T., Gollob, K.J., and Dutra, W.O. (2022). Double-negative T cells: Setting the stage for disease control or progression. Immunology *165*, 371–385.
57. Boots, C.E., and Jungheim, E.S. (2015). Inflammation and Human Ovarian Follicular Dynamics. Semin. Reprod. Med. *33*, 270–275.
58. Umehara, T., Winstanley, Y.E., Andreas, E., Morimoto, A., Williams, E.J., Smith, K.M., Carroll, J., Febbraio, M.A., Shimada, M., Russell, D.L., and Robker, R.L. (2022). Female reproductive life span is extended by targeted removal of fibrotic collagen from the mouse ovary. Sci. Adv. *8*, eabn4564.
59. McCloskey, C.W., Cook, D.P., Kelly, B.S., Azzi, F., Allen, C.H., Forsyth, A., Upham, J., Rayner, K.J., Gray, D.A., Boyd, R.W., et al. (2020).

Metformin Abrogates Age-Associated Ovarian Fibrosis. Clin. Cancer Res. *26*, 632–642.

60. Amargant, F., Manuel, S.L., Tu, Q., Parkes, W.S., Rivas, F., Zhou, L.T., Rowley, J.E., Villanueva, C.E., Hornick, J.E., Shekhawat, G.S., et al. (2020). Ovarian stiffness increases with age in the mammalian ovary and depends on collagen and hyaluronan matrices. Aging Cell *19*, e13259.
61. Landry, D.A., Vaishnav, H.T., and Vanderhyden, B.C. (2020). The significance of ovarian fibrosis. Oncotarget *11*, 4366–4370.
62. Mara, J.N., Zhou, L.T., Larmore, M., Johnson, B., Ayiku, R., Amargant, F., Pritchard, M.T., and Duncan, F.E. (2020). Ovulation and ovarian wound healing are impaired with advanced reproductive age. Aging *12*, 9686–9713.
63. Sánchez-Prieto, M., Sánchez-Borrego, R., Lubián-López, D.M., and Pérez-López, F.R. (2022). Etiopathogenesis of ovarian cancer. An inflamm-aging entity? Gynecol. Oncol. Rep. *42*, 101018.
64. Sun, Y.-C., Wang, Y.-Y., Sun, X.-F., Cheng, S.-F., Li, L., Zhao, Y., Shen, W., and Chen, H. (2018). The role of autophagy during murine primordial follicle assembly. Aging *10*, 197–211.
65. Guo, L., Liu, X., Chen, H., Wang, W., Gu, C., and Li, B. (2022). Decrease in ovarian reserve through the inhibition of SIRT1-mediated oxidative phosphorylation. Aging *14*, 2335–2347.
66. Zhu, J., Yang, Q., Li, H., Wang, Y., Jiang, Y., Wang, H., Cong, L., Xu, J., Shen, Z., Chen, W., et al. (2022). Sirt3 deficiency accelerates ovarian senescence without affecting spermatogenesis in aging mice. Free Radic. Biol. Med. *193*, 511–525.
67. Wang, L.-F., Miao, L.-J., Wang, X.-N., Huang, C.-C., Qian, Y.-S., Huang, X., Wang, X.-L., Jin, W.-Z., Ji, G.-J., Fu, M., et al. (2018). CD38 deficiency suppresses adipogenesis and lipogenesis in adipose tissues through activating Sirt1/PPARγ signaling pathway. J. Cell Mol. Med. *22*, 101–110.
68. Calcaterra, V., Verduci, E., Cena, H., Magenes, V.C., Todisco, C.F., Tenuta, E., Gregorio, C., De Giuseppe, R., Bosetti, A., Di Profio, E., and Zuccotti, G. (2021). Polycystic Ovary Syndrome in Insulin-Resistant Adolescents with Obesity: The Role of Nutrition Therapy and Food Supplements as a Strategy to Protect Fertility. Nutrients *13*, 1848. https://doi.org/10.3390/nu13061848.
69. van Helden, J., Evliyaoglu, O., Küberl, A., and Weiskirchen, R. (2020). Disorders of the glucose metabolism correlate with the phenotype and the severity in women with polycystic ovary syndrome. Clin. Endocrinol. *93*, 44–51.
70. Tolomeo, S., Chiao, B., Lei, Z., Chew, S.H., and Ebstein, R.P. (2020). A Novel Role of CD38 and Oxytocin as Tandem Molecular Moderators of Human Social Behavior. Neurosci. Biobehav. Rev. *115*, 251–272.
71. Dogan, S., Deshpande, D.A., White, T.A., Walseth, T.F., and Kannan, M.S. (2006). Regulation of CD 38 expression and function by steroid hormones in myometrium. Mol. Cell. Endocrinol. *246*, 101–106.
72. Craciunas, L., Tsampras, N., Kollmann, M., Raine-Fenning, N., and Choudhary, M. (2021). Oxytocin antagonists for assisted reproduction. Cochrane Database Syst. Rev. *9*, CD012375.
73. Pierzynski, P., Reinheimer, T.M., and Kuczynski, W. (2007). Oxytocin antagonists may improve infertility treatment. Fertil. Steril. *88*, 213.e19–213.e22.
74. Follicle Selection in Mammalian Ovaries (2019). The Ovary (Academic Press), pp. 3–21.
75. Zhou, C., Wang, W., Peretz, J., and Flaws, J.A. (2015). Bisphenol A exposure inhibits germ cell nest breakdown by reducing apoptosis in cultured neonatal mouse ovaries. Reprod. Toxicol. *57*, 87–99.
76. Wang, Y.-Y., Sun, Y.-C., Sun, X.-F., Cheng, S.-F., Li, B., Zhang, X.-F., De Felici, M., and Shen, W. (2017). Starvation at birth impairs germ cell cyst breakdown and increases autophagy and apoptosis in mouse oocytes. Cell Death Dis. *8*, e2613.
77. Wang, S., Sun, M., Yu, L., Wang, Y., Yao, Y., and Wang, D. (2018). Niacin Inhibits Apoptosis and Rescues Premature Ovarian Failure. Cell. Physiol. Biochem. *50*, 2060–2070.
78. Wang, F., Flanagan, J., Su, N., Wang, L.-C., Bui, S., Nielson, A., Wu, X., Vo, H.-T., Ma, X.-J., and Luo, Y. (2012). RNAscope: A Novel in Situ RNA Analysis Platform for Formalin-Fixed, Paraffin-Embedded Tissues. J. Mol. Diagn. *14*, 22–29.
79. Rueden, C.T., Schindelin, J., Hiner, M.C., DeZonia, B.E., Walter, A.E., Arena, E.T., and Eliceiri, K.W. (2017). ImageJ2: ImageJ for the next generation of scientific image data. BMC Bioinf. *18*, 529.

STAR★METHODS

KEY RESOURCES TABLE

REAGENT or RESOURCE	SOURCE	IDENTIFIER
Antibodies		
Rabbit monoclonal recombinant anti-CD38 antibody	Abcam	RRID:AB_216343
Rabbit monoclonal recombinant anti-DDX4/ MVH antibody	Abcam	RRID:AB_270534
Goat Anti-Rabbit IgG Antibody (H + L), Biotinylated, R.T.U.	Vector Laboratories	RRID:AB_BP-9100-50
Rat monoclonal anti-F4/80 (BM8), Pacific Orange Antibody	Abcam	CAT # ab6640; RRID:AB_1140040
Rat monoclonal anti-CD31 antibody	American Research Products, Inc.	RRID:AB_DIA-310
Goat anti-rabbit IgG (H + L) Highly Cross-Adsorbed Secondary antibody, Alexa Fluor 488	Thermo Fisher Scientific	CAT # A11034; RRID:AB_2576217
Donkey anti-Rat IgG (H + L) Highly Cross-Adsorbed Secondary Antibody, Alexa Fluor Plus 555	Thermo Fisher Scientific	CAT # A48270; RRID:AB_2896336
4′,6-diamidino-2-phenylindole	Invitrogen	RRID:AB_D1306
Rat Monoclonal anti-GCNA1 antibody [TRA98]	Abcam	CAT # ab82527; RRID:AB_1659152
Rabbit monoclonal recombinant anti-DDX4/ MVH antibody	Abcam	RRID:AB_270534
Anti-rabbit IgG, HRP-conjugated secondary antibody	Cell Signaling Technology	RRID:AB_7074V
Mouse beta actin monoclonal antibody (BA3R), HRP	Fisher Scientific	RRID:AB_MA515739HRP
BD OptiBuild™ BUV615 Rat Anti-Mouse CD279 (PD-1)	BD OptiBuild	RRID:AB_752354
BD Horizon™ BUV737 Hamster Anti-Mouse CD27	BD Horizon	RRID:AB_612831
BD OptiBuild™ BUV805 Rat Anti-Mouse Ly-6G and Ly-6C	BD OptiBuild	RRID:AB_741920
BD OptiBuild™ BUV496 Rat Anti-Mouse I-A/I-E	BD OptiBuild	RRID:AB_750171
Brilliant Violet 421™ anti-mouse CD21/CD35 (CR2/CR1) Antibody	BioLegend	CAT # 123422; RRID:AB_2650891
Brilliant Violet 605™ anti-mouse NK-1.1 Antibody	BioLegend	CAT # 108753; RRID:AB_2686977
Brilliant Violet 650™ anti-mouse CD4 Antibody	BioLegend	CAT # 100469; RRID:AB_2783035
Brilliant Violet 711™ anti-mouse CD62L Antibody	BioLegend	CAT # 104445; RRID:AB_2564215
Brilliant Violet 785™ anti-mouse CD138 (Syndecan-1) Antibody	BioLegend	CAT # 142534; RRID:AB_2814047
Pacific Blue™ anti-mouse CD38 Antibody	BioLegend	CAT # 102719; RRID:AB_10613289
BD Horizon™ BV480 Rat Anti-Mouse F4/80	BD Horizon	RRID:AB_565635
Brilliant Violet 510™ anti-mouse CD45 Antibody	BioLegend	CAT # 103137; RRID:AB_2561392

(*Continued on next page*)

Continued

REAGENT or RESOURCE	SOURCE	IDENTIFIER
FITC anti-mouse CD8a Antibody	BioLegend	CAT # 100706; RRID:AB_312745
PerCP/Cyanine5.5 anti-mouse/human CD11b Antibody	BioLegend	CAT # 101227; RRID:AB_893233
CD163 Monoclonal Antibody (TNKUPJ), PerCP-eFluor™ 710, eBioscience	Invitrogen	RRID:AB_46-1631-80
PE anti-mouse CD127 (IL-7Rα) Antibody	BioLegend	RRID:AB_158204
PE/Fire™ 810 anti-mouse CD11c Recombinant Antibody	BioLegend	CAT # 161105; RRID:AB_2904307
PE/Dazzle™ 594 anti-mouse CD19 Antibody	BioLegend	CAT # 115553; RRID:AB_2564000
CD31 (PECAM-1) Monoclonal Antibody (390), PE-Cyanine7, eBioscience™	Invitrogen	RRID:AB_25-0311-81
APC Anti-mouse TCR γ/δ Antibody	BioLegend	CAT # 118115; RRID:AB_1731824
Alexa Fluor® 647 anti-mouse IgD Antibody	BioLegend	CAT # 405707; RRID:AB_893529
Alexa Fluor® 700 anti-mouse CD68 Antibody	BioLegend	CAT # 137025; RRID:AB_2783096
APC/Cyanine7 anti-mouse IgM Antibody	BioLegend	CAT # 406515; RRID:AB_10690815
APC/Fire™ 810 anti-mouse CD3 Antibody	BioLegend	RRID:AB_100268
BD Horizon™ BUV563 Rat Anti-Mouse Ly-6G	BD Horizon	RRID:AB_612921
Chemicals, peptides, and recombinant proteins		
Modified Davidson's Fixative	Electron Microscopy Sciences	64133–50
70% Ethanol	IBI Scientific	IB 15727
Citrisolv Clearing Agent	Fisher Scientific	22-143-975
Xylene	VWR	1330-20-7
Antigen Unmasking Solution	Vector Laboratories	H-3301-250
Tris-Buffered Saline (TBS-10X)	Cell Signaling Technology	12498
Tween® 20	Sigma-Aldrich	P1379-1L
BLOXALL® Endogenous Blocking Solution, Peroxidase and Alkaline Phosphatase	Vector Laboratories	SP-6000-100
Normal Goat Serum Blocking Solution	Vector Laboratories	S-1000-20
Bovine Serum Albumin - Fraction V	Rockland	BSA-1000
Modified Mayer's Hematoxylin	StatLab	HXMMHGAL
Acetic acid	Sigma-Aldrich	27225-1L-R
Fisher Scientific PROTOCOL Bluing Agent	Fisher Scientific	23 245681
Eosin Y Stain	StatLab	STE0150
Sudan Black B	Sigma-Aldrich	50395
ProLong Gold Antifade Reagent	Cell Signaling Technology	9071
Citric Acid	Sigma-Aldrich	C-0759
Sodium Citrate	Sigma-Aldrich	S-4641
Phosphate Buffered Saline, Powdered, Ultra Pure Grade	VWR	97062–336
RIPA Buffer	Thermo Fisher Scientific	89900
1X Halt protease and phosphatase inhibitor cocktail	Thermo Fisher Scientific	78447
4x Laemmli Sample Buffer	Bio-Rad	1610747
2-Mercaptoethanol	Sigma-Aldrich	M6250
Prestained Protein Marker	Thermo FIsher Scientific	26617

(*Continued on next page*)

Continued

REAGENT or RESOURCE	SOURCE	IDENTIFIER
4-20% Mini-PROTEAN TGX Precast Protein Gel	Bio-Rad	4561094
Sodium Chloride	Sigma-Aldrich	S9888
Tris 1.0 M Sterile Solution, pH 7.5 Ultra Pure Grade	VWR	97062–936
Tween 20	Sigma-Aldrich	9005-64-5
1X Turbo buffer	Bio-Rad	10026938
0.2 μm midi-size nitrocellulose membrane	Bio-Rad	1620112
Trans-Blot Turbo Midi-size Transfer Stacks	Bio-Rad	L002044B
1X Tris-Buffered Saline	Cell Signaling Technology	12798
Blotting-Grade Blocker	Bio-Rad	1706404
BSA	Rockland	BSA-1000
Thermo Scientific PLUS Western Blot Stripping Buffer Restore Plus	Fisher Scientific	PI46430
Collagenase IV	Sigma-Aldrich	NC0217889
DNAse I	Sigma-Aldrich	50-178-0833
Olympus Advanced Cell Strainer, 70 μm filter	Genesee Scientific	25–376
Ammonium-Chloride-Potassium ACK lysis buffer	Thermo Fisher Scientific	A1049201
Fc Block	BioLegend	156604
Dialyzed fetal bovine serum	Cytiva Life Sciences	SH30079.01
Sodium azide	Sigma-Aldrich	S2002
13C NAD+	Cambridge Isotope Laboratories Inc.	CLM-10671-PK
13C NAM	Cambridge Isotope Laboratories Inc.	CLM-9925-PK
Nicotinamide adenine dinucleotide	Sigma-Aldrich	N0632
Nicotinamide	Sigma-Aldrich	72340
Adenosyl diphosphate phosphoribose	Sigma-Aldrich	A0752
Ammonium Acetate	Sigma-Aldrich	73594-25G-F
Ammonium Hydroxide	Sigma-Aldrich	AC460801000
HPLC-grade water	Fisher Scientific	W5-4
Acetonitrile (HPLC grade)	Fisher Scientific	A998-4
Methanol (HPLC grade)	Fisher Scientific	600943
Radiance Chemiluminescent Substrate	Fisher Scientific	AC2101
250 mM Sucrose	Sigma Aldrich	57-50-1
40 mM Tris pH 7.5	VWR	97062–936
78c	CalbioChem	5.38763.0001
Nicotinamide 1,N6-ethenoadenine dinucleotide	Sigma Aldrich	N2630
Critical commercial assays		
Avidin/Biotin Blocking Kit	Vector Laboratories	SP-2001
VECTASTAIN Elite ABC-HRP Kit, Peroxidase (Rabbit IgG)	Vector Laboratories	PK-6101
ImmPACT DAB Substrate Kit, Peroxidase (HRP)	Vector Laboratories	SK-4105
Pierce BCA Protein Assay Kit	Thermo Fisher Scientific	23225

(*Continued on next page*)

Continued

REAGENT or RESOURCE	SOURCE	IDENTIFIER
LIVE/DEAD™ Fixable Blue Dead Cell Stain Kit	Invitrogen	L34962
RNAscope™ 2.5 HD Assay-Red Kit	Advanced Cell Diagnostics	322350
RNAscope™ Probe- Mm-Cd38	Advanced Cell Diagnostics	513061
RNAscope™ Positive Control Probe- Mm-Ppib	Advanced Cell Diagnostics	313911
RNAscope™ Negative Control Probe- DapB	Advanced Cell Diagnostics	310043
Deposited data		
Metabolomics data	This paper	MassIVE: MSV000092808
Experimental models: Organisms/strains		
C57BL/6J	The Jackson Laboratory	RRID:IMSR_JAX:000664
B6.129P2-*Cd38tm1Lnd*/J	The Jackson Laboratory	RRID:IMSR_JAX:003727
Software and algorithms		
Spectoflo v3.0.3 software	Cytek	
Flowjo software	BD Biosciences	V10.8.1
ZEN 3.4	ZEISS	Blue Edition
EVOS FL Auto	Invitrogen	2.0.2094.0
LCQUAN™ Quantitative Software	Thermo Scientific	LCQUAN25
Xcalibur™ Software	Thermo Scientific	OPTON-30965
Other		
Leica microtome	Leica Biosystems	RM1255
ImmEdge Hydrophobic Barrier PAP Pen	Vector Laboratories	H-4000
Keyence All-in-One Fluorescence Microscope	Keyence	BZ-X800E
Trans-Blot Turbo Transfer System	Bio-Rad	1704150
Azure 600 imaging system	Azure Biosystems	c600
5-laser Cytek Aurora spectral flow cytometer	Cytek Biosciences	16UV-16V-14B-10YG-8R
EVOS FL Auto Cell Imaging system	Thermo Fisher Scientific	AMAFD2000
HYPERCARB 5UM 100 × 2.1 MM COLUMN	ThermoFisher Scientific	35005–102130
Zirconium Oxide Beads	Next Advance	ZROB05
QExactive™ Benchtop Quadrupole-Orbitrap Mass Spectrometer	Thermo Scientific	
Vanquish™ Core HPLC Systems	Thermo Scientific	VQ-CORE-BIN-01
Bullet blender	Next Advance	Storm Pro BT24M
Speed vacuumn concentrator	Thermo Scientific	SPD1030-115V KIT
96 well black plate	Corning	CLS3650

RESOURCE AVAILABILITY

Lead contact

Further information and requests for resources and reagents should be directed to and will be fulfilled by the lead contact, Eric Verdin (Everdin@buckinstitute.org).

Materials availability

This study did not generate new unique reagents.

Data and code availability

- Metabolomics data have been deposited at the Mass Spectrometry Interactive Virtual Environment (MassIVE) repository, developed by the Center for Computational Mass Spectrometry at the University of California San Diego, and can be downloaded using the following link: https://massive.ucsd.edu/ProteoSAFe/dataset.jsp?task=30dcda32355c46e88e33413bae2d56e6. Data are publicly available as of

the date of publication and the MassIVE ID number is listed in the key resources table.All other data reported in this manuscript will be shared by the lead contact upon request.

- This paper does not report original code.
- Any additional information required to reanalyze the data reported in this paper is available from the lead contact upon request.

EXPERIMENTAL MODEL AND STUDY PARTICIPANT DETAILS

Animals

Male and female C57BL/6J (WT) and CD38 KO on a C57BL/6J background mice were obtained from the Jackson Laboratory (Bar Harbor, ME). For general husbandry maintenance of the line, the CD38KO mice are crossed to C57bl6J (WT) mice and maintained as heterozygous mice. For generating large experimental KO cohorts, homozygous mice that were generated from heterozygous breeding of CD38 KO and WT mice were crossed together. To prevent genetic drift, new wild-type C57bl6J mice of young breeding age are purchased from Jax every 10^{th} generation for backcrossing. Mice were bred and maintained at the Buck Institute vivarium with a 12-h light and dark cycle on a standard chow diet. Mice were provided food and water *ad libitum*. Animal euthanasia was performed either as a humane endpoint or according to experimental endpoints. All procedures were performed in accordance with federal guidelines and those set forth by the Buck Institute Institutional Animal Care and Use Committees (IACUC). Ovaries were isolated from the reproductive tract of WT or CD38 KO mice aged at postnatal day 2, or 2-, 5-, 6-, 12-, 12.5- and 20- months old and either flash frozen in liquid nitrogen or placed in fixative for downstream analyses.

METHOD DETAILS

Ovarian tissue fixation, processing, and embedding

Isolated ovaries were fixed in Modified Davidson's Fixative (Electron Microscopy Sciences, Hatfield, PA, 64133-50) for 2 h at room temperature and then at 4°C overnight with gentle agitation. Tissues were then washed in 70% ethanol (IBI Scientific, Dubuque, IA., IB 15727) three times for 10 min each. Tissues were stored in 70% ethanol at 4°C for up to one week until they were processed for paraffin embedding. All paraffin processing was performed by the Buck Institute's Morphology Core using an automatic benchtop tissue processor (Leica Biosystems, Wetzlar, Germany, TP1020). Paraffin-infused ovarian tissues were embedded in paraffin blocks, and tissues were sectioned at 5 micron thickness using a Leica microtome for downstream applications (Leica Biosystems, RM2155).

RNA *in situ* hybridization and transcript quantification

The RNAScope 2.5 HD Red assay kit (Advanced Cell Diagnostics, Hayward, CA, Cat No. 322350) was used to detect Cd38 mRNA transcripts in ovarian sections from n = 4 reproductively young (2-month-old) C57BL6/J mice. All probes, buffers, blocking and amplification reagents were provided by Advanced Cell Diagnostics. Control probes included Ppib (Cat No. 313911) as a positive control and DapB (Cat No. 310043) as a negative control. The experimental probe was specific to base pair 2–926 of the spliced Cd38 mRNA transcript (Cat No. 513061). Control probes were validated first on control slides containing mouse T3T cells provided by Advanced Cell Diagnostics and all probes were subsequently validated in C57BL6/J liver sections where Cd38 has been previously established. The experiment was performed as previously described[60] with the following modifications. In brief, FFPE tissues are 5 μm sections that were deparaffinized in Citrisolv (Fisher Scientific, 22-143-975) followed by dehydration in a graded ethanol series. Tissue sections were incubated in 1X RNAscope Target Retrieval buffer at 100°C for 15 min followed by a wash in deionized water. Sections were immediately treated with RNAscope Protease Plus and incubated for 23 min at 40°C in the HybEZ hybridization oven (ACD). Probe hybridization and amplification were performed according to manufacturer instructions.[78] Sections were then rehydrated in an ethanol series and counterstained for 2 min in 50% Harris Hematoxylin (Fisher Scientific; Waltham, MA, 23 245651) with brief exposure to 0.02% ammonia water (Sigma-Aldrich, St. Louis, MO, 221228). Sections were imaged in brightfield using a 20× objective on a ZEISS Axioscan7 Imaging system (ZEISS, Oberkochen, Germany). Cd38 transcripts were quantified and normalized to structure area using Fiji ImageJ[79] in specific ovarian sub-compartments, including all follicle classes (primordial, primary, secondary, and antral), corpora lutea, the stroma, vasculature, and the ovarian surface epithelium. In brief, ovarian sub-compartments were identified and defined based on characteristic histologic morphology, and regions of interest (ROI) were drawn and measured using the Freehand selection tool. A color deconvolution macro was written to separate the 2.5 HD Red chromogen from the hematoxylin counterstain in all sections. A standard threshold value was established based on a clear Cd38 transcript signal and was used for all measurements. The calculated Cd38 transcript area was then normalized to the sub-compartment specific area to generate Cd38 transcript signal density in each ROI. A single ovarian section from each animal was analyzed and one of each ovary specific compartment was quantified per section.

Colorimetric immunohistochemistry (IHC)

We performed colorimetric IHC to detect CD38 (Abcam, Cambridge, UK, ab216343 1:1000 for 2-month-old ovary and 1:200 for P2 ovary) and DDX4 (Abcam, ab270534 1:2000). Slides were deparaffinized in Citrisolv Clearing Agent (Fisher Scientific, 22-143-975) or xylene (VWR, Randor, VA, 1330-20-7) and rehydrated in a series of graded ethanol washes (100%, 95%, 85%, 70%, and 50%) that were diluted from 100% ethanol (VWR, 71002-512). Antigen retrieval was performed using an Antigen Unmasking Solution according to the manufacturer's instructions (Vector Laboratories, Newark, Ca, H-3301-250). Slides were washed with 1X Tris-buffered saline (TBS) (Cell Signaling Technology, Danvers, MA, 12498) with 0.1% Tween 20 (Sigma-Aldrich, P1379-1L) (TBST) twice for 15 min and then incubated in BLOXALL Endogenous Blocking Solution,

Peroxidase and Alkaline Phosphatase (Vector Laboratories, SP-6000-100) for 15 min at room temperature. Slides were rinsed in TBS and blocked using an avidin/biotin blocking kit (Vector Laboratories, SP-2001). Slides were then rinsed in TBS and the area around the tissue was defined using a ImmEdge Hydrophobic Barrier PAP Pen (Vector Laboratories, H-4000). Slides were incubated in protein block solution (10% normal goat secondary serum (Vector Laboratories, S-1000) in 3–5% Bovine Serum Albumin - Fraction V in -1X TBS for 1 h (Rockland, Baltimore, MD, BSA-1000). Block was removed and slides were incubated in the respective primary antibody diluted in protein block solution for 1 h or overnight in a humidified chamber. Slides were washed three times in TBST for 5 min each and then incubated with a drop of Goat Anti-Rabbit IgG Antibody (H + L) biotinylated Ready to Use Secondary, (Vector Laboratories, BP-9100-50, undiluted) for 1 h at room temperature. Slides were then incubated with avidin/biotin complex (ABC) (Vector Laboratory, PK-6101) according to manufacturer's instructions. Detection was then performed using a DAB Peroxidase (HRP) Substrate Kit (Vector Laboratories, SK-4105) according to manufacturer's instructions. DAB substrate reaction was stopped by incubating in dH20 for 5 min. Slides were then subjected to a hematoxylin counterstain by incubating slides in the following solutions for described times: 2 min in Modified Mayer's Hematoxylin (StatLab, McKinney, TX, HXMMHGAL), 2 washes with dH20, 1 min incubation in 10% Acetic acid (Sigma-Aldrich, 27225-1L-R), 2 washes with dH20, 2 min in bluing reagent (Fisher Scientific, 23 245681), rinse in dH20, 1 min in 70% ethanol, 1 min in Eosin Y Stain (StatLab, STE0150), rinse in increasing grades of ethanol baths (90%, 95%, 100%), and finally cleared in two Xylene baths. Finally, slides were mounted and coverslipped. Slides were cured overnight and then brightfield images scans were taken with 20X or 40× objectives using either the ZEISS Axioscan 7 Imaging system or the Keyence All-in-One Fluorescence Microscope (Keyence, Itasca, IL, BZ-X800E).

Immunofluorescence

We performed immunofluorescence in ovarian sections to determine co-labeling of CD38 with either F4/80 (Abcam, ab6640 1:200) or CD31 (ARP American Research Products, Waltham, MA, DIA-310 1:20). Histological sections were subject to the same deparaffinization, rehydration, antigen retrieval, and protein blocking steps as previously described. Block was removed and slides were incubated in the respective primary antibodies diluted in the protein block solution overnight in a humidified chamber. The primary antibodies were then removed and sections were washed with TBST three times for 5 min each. Sections were then incubated with goat Alexa 488 and goat Alexa 555 fluorophore-conjugated secondary antibodies (Invitrogen, Waltham, MA, A11034, Thermo FIsher Scientific i 1:1000) diluted in the protein block solution for 1 h at room temperature in a humidified chamber. Sections were then washed three times for 5 min each with TBST. Tissues were then stained with 4',6-diamidino-2-phenylindole (DAPI) (Invitrogen, D1306, 1:5000) for 5 min to visualize DNA. Sections were then washed three times for 5 min each with TBST. Slides were dehydrated in 70% ethanol for 2 min and incubated in Sudan Black B (SBB) to block endogenous autofluorescent lipofuscin accumulation in the ovary (Sigma-Aldrich, 50395, 1:100) for 5 min. Slides were washed with 70% ethanol to remove all SBB and subsequently washed three times with TBST for 5 min each. Slides were then mounted with ProLong Gold Antifade Reagent and allowed to cure overnight (Cell Signaling Technology, 9071). Slides were imaged using the Keyence Microscopy Imaging System with a 40× objective.

In an effort to access the initial primordial follicle reserve, postnatal day two ovaries were collected from CD38 KO and WT female pups and stained for Anti-GCNA1 (Tra98) (Abcam, ab82527, 1:500) and anti-DDX4/MVH (VASA) (Abcam, ab270534, 1:500) in accordance with approved IACUC euthanasia protocol. All fixing, sectioning, staining and mounting procedures were conducted in the same manner as previously described; however, the following changes were applied. Antigen retrieval was conducted using a citrate buffer (created in house from Citric Acid (Sigma-Aldrich, C-0759) and Sodium Citrate (Sigma-Aldrich, S-4641) diluted in dH20). All wash steps were completed using 1X Phosphate Buffered Saline (PBS), Powdered, Ultra Pure Grade (VWR, 97062-336) resuspended in dH20. The same secondary antibodies were used as described previously, however, a 1:200 dilution was used. Sections were imaged using the Keyence All-in-One Fluorescence Microscope at the 40× objective. Quantification of VASA-positive and TRA98-positive germ cells was performed using Imaris v9.9 (Bitplane). After converting files with Imaris converter for downstream analysis, they were imported into Surpass mode and germ cells were manually selected with the spot module. Positive germ cell numbers for VASA and TRA98 immunofluorescence labeling were imported to Microsoft Office Excel. A measurement of the XY diameter of oocytes in the medullary region of P2 ovaries was conducted with ZEN 3.0 (blue edition). From the measurement tab of the software, the line drawing option was selected. In order to measure each oocyte twice, two lines were drawn from four distant points. An average XY value was calculated for each oocyte after importing XY values (in pixels) into Microsoft Office Excel. Statistical analysis was performed using Prism software. t-test was used for analyzing VASA-positive and TRA98-positive germ cell numbers and XY diameters of oocytes between two genotypes.

Immunoblot analysis

Previously frozen whole ovary tissue was lysed in RIPA buffer (Thermo Fisher Scientific, Waltham, MA, 89900) containing 1X Halt protease and phosphatase inhibitor cocktail (Thermo Fisher Scientific, 78447) and lysed using a handheld homogenizer. Samples were incubated on ice for 30 min and then were centrifuged at 4°C and 12,000 rpm for 10 min. The supernatant was then transferred to a pre-chilled new tube. Samples were diluted 1:10 in an RIPA cocktail buffer, and protein concentrations were determined using a Pierce BCA Protein Assay Kit (Thermo Fisher Scientific, 23225). Approximately 30 μg of ovarian lysate was combined with a 4x Laemmli Sample Buffer (Bio-Rad, Hercules, CA, 1610747) prepared with 2-Mercaptoethanol (Sigma-Aldrich, M6250-250 mL) according to the manufacturer's instructions. Samples were mixed well and denatured at 95°C for 5 min. A prestained protein marker (Thermo Fisher Scientific, 26617) and samples were loaded into individual wells of a 4–20% Mini-PROTEAN TGX Precast Protein Gel (Bio-Rad, 4561094). The gel was run in a running buffer (made in house from Sodium Chloride (Sigma-Aldrich, S9888-25G), Tris 1.0 M Sterile Solution, pH 7.5 Ultra Pure Grade (VWR, 97062-936), and Tween 20 (Sigma-Aldrich,

9005-64-5) at 110V until the dye front ran off the gel. The gel was then placed in a 1X Turbo buffer (Bio-Rad, 10026938) and transferred to a 0.2 μm midi-size nitrocellulose membrane (Bio-Rad, 1620112) sandwiched between layers of Trans-Blot Turbo Midi-size Transfer Stacks (Bio-Rad, L002044B) via a semi-dry transfer using a Trans-Blot Turbo Transfer System (Bio-Rad, 1704150). The membrane was washed three times with a 1X Tris Buffered Saline (TBS) (Cell Signaling Technology, 12798) and Tween 20 (Sigma-Aldrich, 9005-64-5) (TBST) for 5 min each and then blocked for 1 h in 0.5% Blotting-Grade Blocker (Bio-Rad, 1706404) diluted in TBST at room temperature. The membrane was then washed three times in the wash buffer for 5 min each and incubated overnight with the same CD38 primary antibody as previously mentioned (1:1000) diluted in 5% BSA (Rockland, BSA-1000) in TBST at 4°C. The membrane was then washed three times in the wash buffer for 5 min each and incubated for 1 h at room temperature with agitation in an anti-rabbit HRP-conjugated secondary antibody (Cell Signaling Technology, 7074V, 1:1000) diluted in the wash buffer. The membrane was washed three times for 5 min each in the wash buffer. The HRP substrate (Fisher Scientific, AC2101) was then prepared and added to the membrane according to the manufacturer's instructions, and the membrane was exposed and imaged using the Azure 600 imaging system (Azure Biosystems, Dublin, CA, c600). The membrane was washed and stripped using a Thermo Scientific PLUS Western Blot Stripping Buffer Restore Plus according to the manufacturer's instructions (Fisher Scientific, PI46430). The membrane was then blocked, washed, and re-probed with a beta actin-HRP conjugated antibody (Fisher Scientific, MA515739HRP 1:1000) as described above, and re-imaged using the same Azure imaging system. Images were then analyzed in Fiji ImageJ to quantify relative amounts of the protein bands. The values of the CD38 bands were normalized to the corresponding housekeeping β-actin bands.

In-silico analysis of publicly available ovarian bulk RNAseq data

A previously published mouse ovaries bulk RNAseq dataset was used for in-silico analysis of changes in CD38 expression in the mouse ovary across the reproductive lifespan. The previously published dataset (Zhang et al., Reproduction 2020) was obtained and downloaded from Buck Institute GCRLE database. The list of 22,086 gene markers was assessed for genes of interest and the average number of Cd38 transcripts per ovary was determined for mice at 3, 6, 9, 12, 15, and 18 months of age (n = 3).

Whole ovary tissue hydrolase activity assay

Measurement of NAD+ hydrolase activity from ovaries collected from mice of different ages was performed using a fluorescence-based NADase activity assay. Ovaries were harvested from WT female mice at 2, 7 and 12 months of age (n = 2) and a CD38 KO female mouse at 2 months of age (n = 2). Ovaries from the same animal were pooled and run as a single sample. After collection, ovaries were placed in a sucrose buffer (250 mM Sucrose (Sigma Aldrich, 57-50-1), 40 mM Tris pH 7.5 (VWR, 97062-936) with 1X Halt protease and phosphatase inhibitor Cocktail (Thermo Fisher Scientific, 78447 suspended in milliQ water) on ice. Tissues were then homogenized with beads in a bullet blender at speed 8 for 5 min. Samples were centrifuged for 10 min at 4°C and 13.8 G and supernatant transferred to a new pre-chilled tube. Protein measurement was performed using the Pierce BCA Protein Assay Kit (Bio-Rad, 23225) following manufacturer's provided protocol. From here, 33 μg of protein in 44 μl of sucrose buffer per sample were transferred in a 96 well black plate (Corning, CLS3650). One ul of DMSO or 78c (CalbioChem, San Diego, Ca, 5.38763.0001) at 50 nM to reach a final concentration of 10 nM was added. Sucrose buffer with DMSO was used as blank control. Five μL of Nicotinamide 1,N6-ethenoadenine dinucleotide (Sigma Aldrich, N2630) 0.8 mM was added to reach the final concentration of 80 μM and start the reaction. The CLARIOstar Plus plate reader (BMG Labtech, Ortenberg, Germany) was used to measure fluorescence at 300 nm excitation and 410 nm emission every 60 s for 1 h. Following assay completion, the NADase activity was extrapolated as the slope of the linear portion of the Fluorescence over time curve.

LCMS analysis of the ovary

Measurement of NAD+ and related metabolites from flash frozen ovaries collected from mice of different ages and at the end of the breeding trial was performed via LCMS analysis. Briefly, each ovary was homogenized in a bullet blender, vortexed for 10 s and incubated for 30 min on ice. Upon centrifugation at 18,000 rcf for 10 min, the supernatant was transferred to a new eppendorf tube and dried in a speed vacuum. The final dried pellet was resuspended in starting buffer conditions for subsequent LCMS analysis. 13C NAD+ and 13C NAM (Cambridge isotope laboratories Inc. MA, USA, CLM-10671-PK and CLM-9925-PK) were used as internal standards. Ovary extracts were analyzed with QExactive Mass Spectrometer coupled to a Vanquish LC system (Thermo Scientific). Separation of metabolites was achieved in 12 min using a Hypercarb column (5 mm, 100 × 2.1 mm column, Thermo Scientific) and a gradient run of solvent A (7.5 mM ammonium acetate with 0.05% ammonium hydroxide) and solvent B (0.05% ammonium hydroxide in acetonitrile). The gradient program was as follows: 0–1 min, 5% B; 6 min, 60% B; 6.1–7.5 min, 90% B; 7.6–12 min, 5% B. Data acquisition was performed using FullMS1-ddMS2 (Top4) within a scan range of 50–750 m/z, with a resolution of 70000, AGC target of 1e6, and a maximum IT of 100 ms. Relative levels of respective metabolites in the ovary were measured using their MS1 extracted ion chromatogram and corresponding normalized AUC. Metabolite identification was confirmed with corresponding retention time and MS2 fragmentation spectra of metabolite standards run in parallel. To compute quantitative levels, an 8-point calibration curve of pooled NAD+, NAM and ADPR standards (Sigma Aldrich, N0632, 72340, A0752 respectively) was prepared, extracted, and analyzed alongside ovary extracts. Frozen ovary weights were used to normalize to represent quantitative data as pmol/mg ovary. Aged ovaries that were too small, with corresponding inaccurate weights, were excluded.

Flow cytometry

Both ovaries from each mouse were pooled and processed for flow cytometric analysis. Isolated ovaries were cut into small pieces and sequentially incubated in collagenase IV (Sigma-Aldrich, NC0217889) and DNAse I (Sigma-Aldrich, 50-178-0833) for 30 min and 15 min, respectively, in a 37°C dry bath with gently mixing. Each homogenate was then passed through an Olympus Advanced Cell Strainer, 70 μm filter (Genesee Scientific, 25–376) and the resulting filtrate was subjected to three rounds of gentle washes with PBS and centrifugation, with an incubation with Ammonium-Chloride-Potassium ACK lysis buffer (Thermo Fisher Scientific, A1049201) for 5 min between the last two washes. Ovarian cell suspensions were then seeded in 96-well V-bottom plates and incubated with LIVE/DEAD Fixable Blue Dead Cell Stain Kit (Invitrogen, L34962, 1:2000) and Fc Block (BioLegend, San Diego, CA, clone S17011E, 156604) for 25 min at 4°C. Next, samples were stained in the staining buffer (PBS containing 1% Dialyzed fetal bovine serum (Cytiva Life Sciences, Marlborough, MA, SH30079.01), 0.09% sodium azide (Sigma-Aldrich, S2002) using the following antibody panel: PD-1-BUV615 (BD OptiBuild, clone RMP1-30, 752354, 1:50); CD27-BUV737 (BD Horizon, clone LG.3A10, 612831, 1:200), Ly-6C/g-BUV805 (BD OptiBuild, clone RB6-8C5, 741920, 1:200); Class II-BUV496 (BD OptiBuild, clone 2G9, 750171, 1:200); CD21/35- BV421 (BioLegend, clone 7E9, 123422, 1:200); NK1.1-BV605 (BioLegend, clone PK136, 108753, 1:200); CD4-BV650 (BioLegend, clone GK1.5, 100469, 1:200); CD62L- BV711 (BioLegend, clone MEL-14, 104445, 1:400); CD138- BV785 (BioLegend, clone 281-2, 142534, 1:800), CD38-Pac Blue (BioLegend, clone 90, 102719, 1:400); F4/80-BV480 (BD Horizon, clone T45-2342, 565635, 1:200); CD45-BV510 (BioLegend, clone 30-F11, 103137, 1:200), CD8-FITC (BioLegend, clone 53–6.7, 100706, 1:200); CD11b-PerCP-Cy5.5 (BioLegend, clone M1/70, 101227, 1:400), CD163-PerCP-eFluor_710 (Invitrogen, clone TNKUPJ, 46-1631-80, 1:200), CD127- PE (BioLegend, clone S18006K, 158204, 1:400), CD11c-PE-Fire_810 (BioLegend, clone QA18A72, 161105, 1:200), CD19-PE-Dazzle_594 (BioLegend, clone 6D5, 115553, 1:200), CD31-PE-Cy7 (Invitrogen, clone 390, 25-0311-81, 1:200), TCRgd- APC (BioLegend, clone GL3, 118115, 1:400); IgD- Alexa _Fluor_647 (BioLegend, clone 11-26c.2a, 405707, 1:800), CD68-AF700 (BioLegend, clone FA-11, 137025, 1:200); IgM-APC-Cy7 (BioLegend, clone RMM-1, 406515, 1:200); CD3-APC-Fire_810 (BioLegend, clone 17A2, 100268, 1:200); LY6G-BUV563 (BD Horizon, clone 1A8, 612921, 1:200). Staining was done at 4°C for 30 min. Flow cytometry acquisition was done using a 5-laser Cytek Aurora spectral flow cytometer (Cytek Biosciences, Fremont, CA, 16UV-16V-14B-10YG-8R). Spectral Unmixing was done using Spectoflo v3.0.3 software of Cytek and further flow analysis and UMAP plots were done using Flowjo software (BD Biosciences, Franklin Lakes, NJ, V10.8.1).

MNGC quantification

For multinucleated giant macrophage cell (MNGC) quantification, 1545 H&E stained ovarian sections from 2, 5, 12.5, 20, and 28 month old C57BL6/J WT (n = 5, 4, 4, 4, 5; respectively) and CD38 KO (n = 5, 5, 5, 4, 5; respectively) mice were analyzed to compare observable temporospatial macrophage dynamics in these groups. To address the variable intensity of staining, section images were adjusted by shifting intensities such that the mean margin intensity was set to a baseline value. The presence of MNGCs was visually determined according to previously published criteria 33. Quantification of the MNGC area was performed in Fiji ImageJ using an automated batch script to separate yellow MNGC signal from the remainder of the H&E stain using a color deconvolution macro and measure the extent of MNGC structures using a common threshold. Ovarian section area was also measured using threshold adjustment and MNGC area was reported as a % of section area. On average, 34 sections were analyzed from each ovary, and the mean percent of section area was determined to generate ovarian MNGC area density for each animal.

Follicle classification and counting

Follicle classification and counting was performed to quantify ovarian reserve and activated follicles in WT and CD38 KO ovaries across the reproductive lifespan. Serial sections from 2, 5, 12.5, 20, and 28 month old C57BL6/J WT (n = 5, 4, 4, 4, 5; respectively) and CD38 KO (n = 5, 5, 5, 4, 5; respectively) were stained with Hematoxylin and Eosin (H&E) as described in the "hematoxylin and eosin staining" section. Sections were imaged in brightfield using a 20× objective on a ZEISS Axioscan7 Imaging system and the EVOS FL Auto Cell 2 Imaging system (Invitrogen, Waltham, MA, AMAFD2000). Follicles were classified according to previously published criteria[36] and counted by class specific annotation on ZEISS ZEN 3.4 (blue edition) or EVOS FL Auto 2 Software (Rev. 2.0.2094.0). In brief, primordial follicles were classified as oocytes surrounded by an incomplete or complete layer of squamous granulosa cells. Primary follicles were characterized as oocytes surrounded by a single layer of cuboidal granulosa cells. Primordial and primary follicles were counted irrespective of whether the oocyte nucleus was visible in the section. Secondary follicles were classified as oocytes surrounded by more than one layer of cuboidal granulosa cells. Antral follicles were classified by the presence of a visible antrum and a cumulus oocyte complex surrounded by multiple layers of mural cells. Only secondary or antral follicles with an oocyte nucleus present in the section were included to avoid duplicate counting of these large later stage follicles. Only morphologically normal follicles were counted. Atretic follicles, as distinguished by granulosa cells with pyknotic nuclei and shrunken oocytes with condensed and fragmented chromatin, were not included. The area of each analyzed ovarian section was measured by using the freehand spline tool in ZEN 3.4 (blue edition) or the freehand polygon tool on the EVOS FL AUTO. Follicle counts were normalized to the sum of the areas of all analyzed ovarian sections as a measure of ovarian follicle density. The fraction of each follicle class relative to the total follicle count for each ovary was also reported.

Breeding trial

To assess fertility, a breeding trial was performed in which non-littermates CD38 KO and WT female virgin mice at 2, 6, and 12 (n = 5, 4, 5) months of age were individually housed with 3-month-old WT males (n = 5, 5, 5) of proven fertility for a continuous 6-month period. One

breeding pair from the mid CD38 KO female x WT male group generated no pups throughout the duration of the breeding trial and during the post-breeding trial tissue collection, the female had a large pituitary tumor. Due to this disease state, this breeding pair was excluded from the data analysis. Breeding cages were checked daily, and the number of litters, number of pups born, and pup survival were recorded. Following standard procedures, the pups were left with dams until weaning at postnatal day 21. At the end of the breeding trial, we harvested and flash froze ovaries to assess NAD+.

Hematoxylin and eosin staining

Histological sections were subjected to the same deparaffinization and rehydration as previously described. Slides were incubated with the following protocol: 2 min in Modified Mayer's Hematoxylin (StatLab, McKinney, TX, HXMMHGAL), 2 washes with dH20, 1 min incubation in 10% Acetic acid (Sigma-Aldrich, 27225-1L-R), 2 washes with dH20, 2 min in bluing reagent (Fisher Scientific, 23 245681), rinse in dH20, 1 min in 70% ethanol, 1 min in Eosin Y Stain (StatLab, STE0150), rinse in increasing grades of ethanol baths (90%, 95%, 100%), and finally cleared in two Xylene baths. Finally, slides were mounted, coverslipped, and cured overnight.

QUANTIFICATION AND STATISTICAL ANALYSIS

Unpaired t-test, Paired t-test, two-way ANOVA test and Mann–Whitney test were performed where appropriate as reported in the figure legends. A comparison was considered significant if p values were less than 0.05. All statistical analyses were performed using GraphPad Prism software (Version Version 9.5.1).